Available online at www.sciencedirect.com
SCIENCE DIRECT®
Journal of Computational Physics 213 (2006) 704–729
JOURNAL OF COMPUTATIONAL PHYSICS
www.elsevier.com/locate/jcp

A robust unstructured grid discretization for 3-dimensional hydrostatic flows in spherical geometry: A new numerical structure for ocean general circulation modeling

G.R. Stuhne *, W.R. Peltier

Department of Physics, University of Toronto, 60 St. George Street, Toronto, ON, Canada M5S 1A7

Received 6 May 2005; received in revised form 26 August 2005; accepted 29 August 2005
Available online 7 October 2005

Abstract

Current models of the general circulation of the global oceans employ a spatial discretization of the relevant hydrodynamic fields on Cartesian rectilinear grids. For many applications, significant benefit would be expected to accrue from the versatility offered by unstructured grids. However, until very recently, available numerical methods for performing integrations on unstructured grids could not conserve discrete dynamical invariants, a numerical model characteristic that is important for robust ocean simulations over large space and time scales (as needed, for instance, in climate modeling applications). Our purpose in this paper is to describe such a conservative discretization scheme for rotating hydrostatic Boussinesq fluid dynamics on general triangular tessellations of the sphere, and to demonstrate its properties in a number of simulations that incorporate realistic ocean basin geometry. Several different implicit time discretizations are possible, each of which exhibits a form of exact numerical energy conservation in the absence of dissipation. The properties of this new numerical methodology are validated through analysis of a sequence of unforced nonlinear dynamical problems, which clearly demonstrate the capacity of the model to resolve the geostrophic adjustment process and the onset of baroclinic instability in collapsing density fronts. As a final test, a number of ocean modeling experiments with realistic climatological and wind-stress forcing are performed in order to investigate the manner in which different mesh structures and resolutions influence the simulated phenomenology. As the theoretical properties of the numerical methodology suggest, it is thereby shown to be both robust and stable. The further work that will be required to implement this structure in a state-of-the-art oceanic general circulation model, as well as other potential applications of the techniques, are discussed in the concluding section of the paper.

PACS: 02.70; 89.82

Keywords: Ocean modeling; Unstructured grids; Hydrostatic flows; Spherical geometry; Numerical methods

* Corresponding author. Tel.: +1 416 946 7086; fax: +1 416 978 8905.
E-mail address: gordan@atmosp.physics.utoronto.ca (G.R. Stuhne).

0021-9991/$ - see front matter © 2005 Elsevier Inc. All rights reserved.
doi:10.1016/j.jcp.2005.08.031

1. Introduction

A variety of numerical models of the global ocean circulation and tides have previously been described, but the implementations of these models have historically drawn upon a very limited range of computational techniques. Ever since the early work of Bryan [1] and Bryan and Cox [2], Cartesian curvilinear grids have been used to discretize the dynamical state of the oceans, as determined by the global spatial distributions of velocity and other quantities (see, e.g., the historical review by Semtner [3] and the text by Griffies [4]). The simplest examples of such structured grids derive from regular latitude-longitude coordinates, and therefore exhibit singularities at the north and south poles (which presents a problem as the former lies in the ocean domain). Improved spatial discretizations have been achieved by remapping and reconnecting the basic Cartesian grid topology, which has allowed global ocean modelers not only to circumvent pole problems, but also to perform simulations in which rows and columns of grid points are more finely spaced in specific regions of interest than in the overall domain (e.g., Murray [5]). However, this capability is still very primitive in comparison with so-called unstructured meshing techniques, which have long been used in engineering to facilitate fluid dynamical simulations with complex domain geometries and spatially varying grid resolution.

The advantages of unstructured grid techniques in ocean modeling have already been illustrated in a variety of coastal and regional-scale analyses (see, e.g., Myers and Weaver [6], Lynch et al. [7], Casulli and Walters [8], Chen et al. [9], Nechaev et al. [10], and Zhang et al. [11]). Being defined upon very general spatial discretizations, such techniques make it possible for oceanic models to be closely matched to bathymetry. They allow, for instance, for increased resolution in regions with strong topographic slopes or western boundary currents. Moreover, the edges of cells in an unstructured grid may be more-or-less arbitrarily oriented in space (apart from some modest conditions on topology and element quality), and meshes can therefore be constructed in which regions delimited by specified isobaths are well-represented by sets of undivided cells of the discrete mesh. In particular, the geometry of land–sea boundaries can be represented with greater fidelity by an unstructured grid than by a Cartesian grid of comparable resolution, in which the corners of discretized coastlines must always have approximately 90° angles.

We are interested in the problem of global ocean general circulation modeling, which presents a set of challenges somewhat different from those associated with local modeling. One clearly does not need to specify heuristic lateral boundary conditions where simulated and unsimulated portions of the ocean interact, but must instead derive the model in spherical geometry, making use of a topographic data set (such as ETOPO2 [12]) that covers the entire surface of the Earth. In principle, naïve adaptations of numerical techniques developed for local unstructured grid ocean models could be applied in spherical geometry, but there are problems with such an approach. Whereas local ocean models are typically designed for short simulations (on the order of days to months), ocean general circulation models (OGCMs) are very often used to study dynamics on time scales ranging from years to centuries or even millenia (e.g., see Peltier and Solheim [13]). The computational methods used in the implementation of OCGMs must therefore adequately represent the budgets of important dynamical quantities while ensuring numerical stability for simulations of indefinite duration. Existing OGCMs have fulfilled these conditions to an acceptable degree by exploiting mesh staggering techniques whose application to structured Cartesian grids has long been well-understood. A particularly well-known example of such a Cartesian staggered mesh scheme is that of Harlow and Welch [14], which conserves, among other quantities, the local and global kinetic energy and vorticity (see Lilly [15]). However, the extensions of conservative staggered mesh discretizations to *unstructured* grids have not been described until recently (see Perot [16], Zhang et al. [17] and references therein).

We describe the implementation of a new unstructured grid OGCM based upon a numerical methodology that has analytically verifiable stability and conservation properties. The computational techniques can be applied to a range of geophysical fluid dynamical models, but for initial illustrative purposes we will represent the oceans as a hydrostatic, rigid-lid Boussinesq fluid on the rotating sphere. The methodology fits within a broader class of covolume and unstructured orthogonal mesh techniques that were proposed for the incompressible Navier–Stokes problem by Nicolaides [18], and that have subsequently been generalized for application to local baroclinic coastal models by Casulli and Walters [8] and Zhang et al. [11]. The finite-volume/finite-difference methods of these authors exploit special geometric characteristics of unstructured grids and use a semi-implicit time-stepping scheme that simultaneously determines velocity and pressure. This is inherently

more accurate than the "mode splitting" done by most OGCMs, which tend to use predictor-corrector schemes that decouple barotropic and baroclinic modes in a somewhat ad hoc fashion (e.g., Griffies [4], Chapter 12). However, the coastal models described by Casulli and Walters [8] and Zhang et al. [11] invoke explicit discretizations for advective nonlinear terms, which simplifies the algebraic equations that need to be solved (making them symmetric positive definite, or SPD), but precludes the exact conservation of quadratic invariants such as kinetic energy. Such conservation, which cannot be achieved in any case in models using predictor–corrector strategies (see Bryan and Cox [19]), represents an advantage even over existing Cartesian grid OGCMs.

The numerical methodology described herein enforces the discrete conservation of quadratic invariants on spherical unstructured grids using a generalization of an unstructured mesh staggering technique that Perot [16] has shown to be energy-conserving on flat planar domains. Under appropriately unforced and non-dissipative conditions, energy conservation can be maintained to arbitrary precision when the spatial discretization is combined with a specific type of implicit temporal discretization (whose detailed implementation has apparently not been discussed before). We derive appropriate discretized dynamical equations and evolve them with the aid of a Krylov subspace iteration technique (GMRES [20]), which solves the non-symmetric linear equation systems relating dynamical fields at successive time levels. This is more costly than the use of direct methods without solvers, or methods that use preconditioned conjugate gradient iteration to solve SPD systems, but it brings the benefit that robustness is ensured through the local and global conservation of quadratic quantities that are invariants of the continuous system (to within bounds dependent upon the tolerance used in the algebraic solution).

Conservation of invariants essentially ensures that a limited subset of the discrete degrees of freedom will be accurately resolved. In the broader sense, accuracy is characterized by the order of convergence of solutions with increasing spatial or temporal resolution. Basic analytical considerations, along with results reported by Casulli and Walters [8] and others, suggest that orthogonal unstructured grid techniques are first order in space for arbitrary meshes, but approach second order accuracy when grid cells are regular in shape. The order of convergence of our scheme hence depends upon the details of the techniques used to generate the spherical unstructured grids, a topic that we will touch upon briefly, without going into great detail. Order of accuracy has generally not been of primary concern in OGCMs, and there do not appear to be any global reference solutions against which convergence can be assessed. Efforts to evaluate model performance along these lines were made during the development of atmospheric GCMs (see Williamson et al. [21]), but published discussions of OGCM results tend to focus on phenomenology, and rely upon elaborate initialization and forcing schemes and mixing parameterizations to generate realistic flows. Without addressing in detail the secondary issues that complicate global ocean modeling, we will discuss the results of a number of OGCM-type simulations with climatological buoyancy and wind-stress forcing, assessing how varying mesh structure and resolution affects the resolved phenomenology. Where auxiliary hypotheses are required to close the dynamics, we will consistently invoke common, though not necessarily state-of-the-art, approximations. These test results will demonstrate in a rudimentary way that the numerical methods are accurate, robust and efficient enough to sustain "realistic" OGCM dynamics over useful grid resolutions and time intervals.

The energy budgets of OGCM simulations are generally too complex to permit straightforward quantitative analysis, and in order to evaluate the crucial features of our discretization we also discuss a number of contrived initial value simulations that have simple energy budgets while still exhibiting the important processes of geostrophic adjustment and baroclinic instability. The various test results will be presented in Section 3 below, after we have described the details of the spatial discretization procedure and computational methodology in Section 2. Concluding remarks and a discussion of our plans for future work are provided in Section 4.

2. Model and numerical discretization

2.1. Dynamical equations

The first matter that must be addressed concerns the form in which the equations are written that are to be discretized on the surface of the sphere. As noted, the present work makes use of the 3D hydrostatic and Boussinesq model, although similar issues arise for alternative approximations of the fluid physics. The transport equations for heat and salinity scalars have a straightforward form: i.e.,

$$\begin{aligned}\frac{\partial T}{\partial t} + [\mathbf{v}\cdot\nabla - \mathscr{D}(\mu_\mathrm{h},\mu_\mathrm{v})]T = F_\mathrm{T},\\ \frac{\partial S}{\partial t} + [\mathbf{v}\cdot\nabla - \mathscr{D}(\mu_\mathrm{h},\mu_\mathrm{v})]S = F_\mathrm{S}.\end{aligned} \tag{1}$$

Temperature, T, and salinity, S, evolve according to a pair of forced advection–diffusion systems, with F_T and F_S being the respective forcing terms, while $\mathbf{v}$ is the 3-D advecting velocity field in the spherical shell and $\mathscr{D}(\kappa,\sigma)$ is used to denote a linear diffusion operator. $\kappa = \mu_\mathrm{h}$ is the dissipation coefficient in the horizontal (i.e., tangential) direction, and $\sigma = \mu_\mathrm{v}$ is the corresponding coefficient in the radial direction $\hat{\mathbf{r}}$, with both coefficients varying in space and time in general.

Conceptually, momentum (and hence velocity) in the Boussinesq system could be regarded similarly as evolving by advection–diffusion dynamics, except for a number of complicating issues. Firstly, the velocity field, $\mathbf{v}$, must satisfy the conservation of volume constraint, $\nabla\cdot\mathbf{v} = 0$, which, as is typical in incompressible hydrodynamics, determines the pressure field, p. In *hydrostatic* Boussinesq dynamics, only the horizontal velocity evolves prognostically, while conservation of volume determines the *surface* pressure (for the case of a rigid lid), as well as the vertical velocity, $w \equiv \mathbf{v}\cdot\hat{\mathbf{r}}$. The vertical variation of pressure is determined by the hydrostatic relation: i.e.,

$$\frac{4\pi^2}{\Omega_0^2 r_0 \rho_0}[\hat{\mathbf{r}}\cdot\nabla p + g\rho(T,S,p_*(z))] = \frac{\partial \hat{p}}{\partial z} + \hat{\rho}(T,S,z) = 0, \tag{2}$$

while the volume conservation condition and advection operator are given by

$$\begin{aligned}\nabla\cdot\mathbf{v} &= \nabla\cdot\mathbf{u} + \frac{\partial w}{\partial z} = 0,\\ \mathbf{v}\cdot\nabla &= \mathbf{u}\cdot\nabla + w\frac{\partial}{\partial z},\end{aligned} \tag{3}$$

in which $\mathbf{u} \equiv \mathbf{v} - w\hat{\mathbf{r}}$ is the horizontal velocity. We have introduced a non-dimensionalization whose length unit is the radius of the Earth at sea level, r_0, and the offset vertical coordinate, $z \equiv \sqrt{x^2+y^2+z^2} - 1$, measures the radial displacement of a point with respect to this radius. Unit time is prescribed to be 1 day ($2\pi/\Omega_0$, with Ω_0 the angular velocity of the planet), while the pressure and density are non-dimensionalized as shown in Eq. (2), in which ρ_0 is the Boussinesq reference density, g is the acceleration due to gravity, and the function $p_*(z)$ is an a priori estimate of the variation of pressure with depth. Such a function is conventionally used in order to linearize the determination of the pressure profile from the equation of state. Hereafter, all quantities should be assumed to be non-dimensional, with hats dropped.

An additional factor that complicates the treatment of horizontal momentum evolution in terms of advection and diffusion relates to the fact that this quantity is a 2-D vector on the curved spherical surface. Cartesian grid modelers typically derive discrete conservation laws for u_1 and u_2 in flux form from the 2-D tensor form of the momentum equation, using a basis aligned with the gradients of orthogonal coordinate functions, $\nabla\xi_1$ and $\nabla\xi_2$, which are conveniently approximated by the edges of grid cells (for example, $\nabla\lambda$ and $\nabla\phi$ point north and east if λ and ϕ are latitude and longitude, respectively). This approach is not viable for spherical unstructured grids, which are, by their very nature, not associated with any curvilinear coordinate system. However, an alternative mathematical treatment of the horizontal momentum dynamics entails representing them as a fully three-dimensional flow with a constraining force acting upon the horizontal velocity vector, $\mathbf{u} = u_x\hat{\mathbf{x}} + u_y\hat{\mathbf{y}} + u_z\hat{\mathbf{z}}$, in such a way as to enforce the condition $\mathbf{u}\cdot\hat{\mathbf{r}} = 0$. When the effects of the Coriolis force are also included, the evolution equation for the three components of $\mathbf{u}$ takes the form

$$\frac{\partial \mathbf{u}}{\partial t} + [\mathbf{v}\cdot\nabla - \mathscr{D}(\nu_\mathrm{h},\nu_\mathrm{v}) + 4\pi\hat{\mathbf{z}}\times]\mathbf{u} + \nabla p = \mathbf{F}_\mathbf{u} + \Lambda\hat{\mathbf{r}}, \tag{4}$$

where $\mathbf{F}_\mathbf{u}$, ν_h, and ν_v are the forcing function, horizontal viscosity, and vertical viscosity, respectively.

For the pure horizontal case where $\mathbf{v} \equiv \mathbf{u}$, $\mathscr{D}\mathbf{u} \equiv 0$, $\Lambda = -\mathbf{u}\cdot\mathbf{u}$, and p is governed by shallow-water height field dynamics, Côté [22] has shown that Eq. (4) is equivalent to the tensor form of the momentum equation. For the Boussinesq case, the more complex relation between $\mathbf{u}$ and $\mathbf{v}$ and the corresponding advection operator are given by Eq. (3) but, since $\partial\hat{\mathbf{r}}/\partial z = 0$, the constraint force is unaffected. The form of the spherical momen-

tum diffusion operator raises more subtle issues, and we will not devote a great deal of attention to this problem, which has been handled at various levels of approximation by Cartesian grid ocean models (see Griffies [4], Chapter 19). In any case, our discretization, which projects **u** onto the horizontal faces of grid cells in a natural way, will be seen to eliminate the "extra" degrees of freedom in Eq. (4) and the need to explicitly compute the Lagrange multiplier Λ. We will, however, relate this term to the discretization error associated with spherical curvature (see Section 2.3 below).

2.2. Oceanic grids

In principle, the numerical discretization that is being described can be applied to any spherical triangular tessellation of the ocean domain. The generation of such meshes, given bathymetry data as input, is a subject in itself, and we will not discuss it in any detail here. We have experimented with a number of approaches derived from one or the other of two well-known surface mesh generation techniques: the *advancing front* method (e.g., Lau and Lo [23]), or the *quadtree* method (e.g., Greaves and Borthwick [24]). Described succinctly, the advancing front method entails first computing the coastal contours and discretizing them with edges of desired length. The ocean area is then filled in with triangles by an iterative procedure, each step of which involves the "extrusion" of a triangle into the ocean from one of the coastal edges. This modifies the discrete coastline (or "front") while reducing the size of the untriangulated portion of the ocean domain, which vanishes entirely at the final step of the algorithm. Quadtree methods, in contrast, begin with the construction of a complete, coarse-grain tessellation of the spherical surface into triangles (we use the Platonic spherical icosahedron because it has been found to have favorable geometric properties; see, e.g., Baumgardner and Frederickson [25], Stuhne and Peltier [26,27]). A different kind of iterative procedure is then carried out, each step of which entails subdividing one triangle of the mesh into 4 in order to increase the local resolution (hence "quadtree"). Except in the special case in which the entire mesh has been uniformly subdivided, this results in a non-conformal triangulation that must be corrected by means of a topological balancing procedure. The portion of the triangulation that is not in the ocean is then deleted in the final step of the algorithm.

Fig. 1 compares ocean tessellations that were generated by the two respective methods (the top two frames by advancing front, and the bottom two by quadtree). All cases utilized the ETOPO2 [12] bathymetry database and the left frames show the results when a uniform "target" node spacing of about 2° is prescribed. For the quadtree method, this simply corresponds to a fivefold dyadic refinement of the basic spherical icosahedron, which is illustrated in the lower left frame. The mesh in the upper left frame, which was generated by the advancing front method, has comparable node spacing and very similar total node and triangle counts. However, its qualitative structure is markedly different. The advancing front mesh obviously provides a more faithful representation of the coastline, while the quadtree mesh provides a more regular distribution of triangle shapes and node connectivities. The same continues to hold true when the node spacing is prescribed to be variable over the surface of the sphere, as is the case in the example shown in the two right frames of Fig. 1. For this case, close-ups of the discretization of a portion of the Arctic ocean are depicted.

Clearly, the coastal fidelity offered by the advancing front technique is a desirable feature, while the coastlines of the quadtree meshes continue to exhibit a version of the jagged coastline problem that afflicts regular Cartesian meshes. Unfortunately, the more erratic mesh geometry in the ocean interior often results in poor numerical accuracy, and to date we have obtained robust results using only the quadtree method. There is, however, a wealth of strategies for mesh generation and improvement, and we are, in ongoing work, developing a more optimal combination of techniques. The results to be described in what follows were obtained using quadtree meshes.

2.3. Horizontal discretization

We consider first the uppermost radial level of the discretization, which is a triangular discretization of the spherical shell that represents the entire ocean domain, while excluding those portions of the globe that are above sea level. The material in the first part of this subsection overlaps to some degree with Perot's [16] discretization of the divergence form of the Navier–Stokes equations on the plane. However, we require a more general version of these results that applies to spherical shells, and that can be adapted to the 3-D rotating Boussinesq equation system (see Sections 2.4 and 2.5 below).

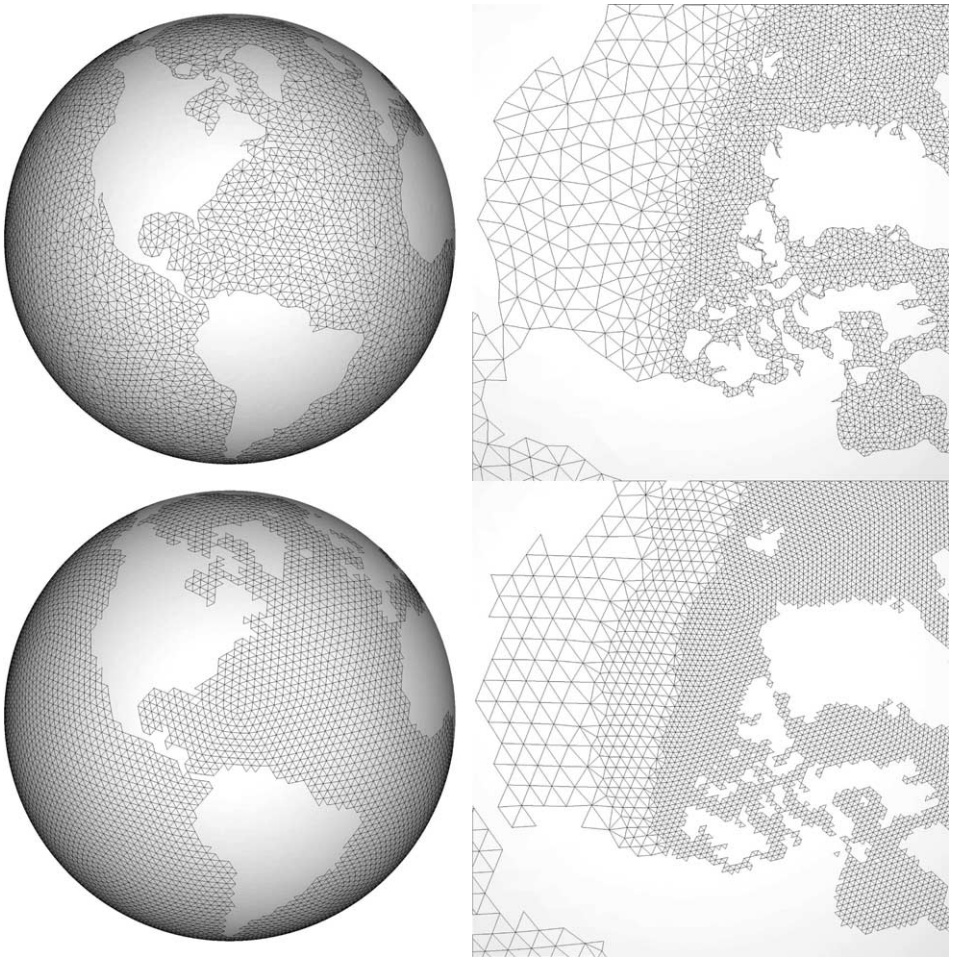

Fig. 1. Illustrations of computational grids generated by advancing front (top) and quadtree (bottom) methods. The left example shows a uniform grid on the full globe, while the right example focuses on a non-uniformly gridded region of the Arctic ocean.

The discretization is based upon cell-edge communication, with quantities being indexed over a set of N_t triangular cells and a set of N_e edges, each of which is adjacent to one or two triangles (two, in the case of an interior edge; and one, in the case of a boundary edge). The topological coincidences of triangle vertices and edge endpoints determine, additionally, a set of N_p nodes at positions $\mathbf{x}_1, \mathbf{x}_2, \ldots, \mathbf{x}_{N_p}$. Supposing that Φ and λ denote "field" quantities tied, respectively, to triangles and edges, the subscripted symbols $\Phi_{\mathbf{c}} = \Phi_{(c_1,c_2,c_3)}$ and $\lambda_{\mathbf{e}} = \lambda_{(e_1,e_2)}$ are used to denote their particular values at given triangles and edges. The integers c_1, c_2, and c_3 in the three-component index, $\mathbf{c}$, of a triangle are the node indices of its vertices, while the integers e_1 and e_2 in the two-component index of an edge, $\mathbf{e}$, are the node indices of its endpoints. If c_i and c_j are two different corners of triangle $\mathbf{c}$, then there is a unique edge, $\mathbf{e}$ – either (c_i, c_j) or (c_j, c_i) – linking them in the direction prescribed by the order of indices in $\mathbf{e}$. The orientations of edges are arbitrary in relation to the geometry, while the components of triangle indices, $\mathbf{c}$, are in such order that the triangle has positive orientation with respect to the local surface normal: i.e.,

$$\mathbf{x}_{c_1} \cdot [(\mathbf{x}_{c_2} - \mathbf{x}_{c_1}) \times (\mathbf{x}_{c_3} - \mathbf{x}_{c_1})] > 0. \tag{5}$$

The geometry and indexing scheme of the discretization is illustrated in Fig. 2, which shows four neighboring spherical triangles and adjacent edges, along with some geometric quantities tied to these objects. $\bar{\mathbf{x}}$ and $\hat{\mathbf{n}}$ denote the midpoints and normals of edges, as determined by

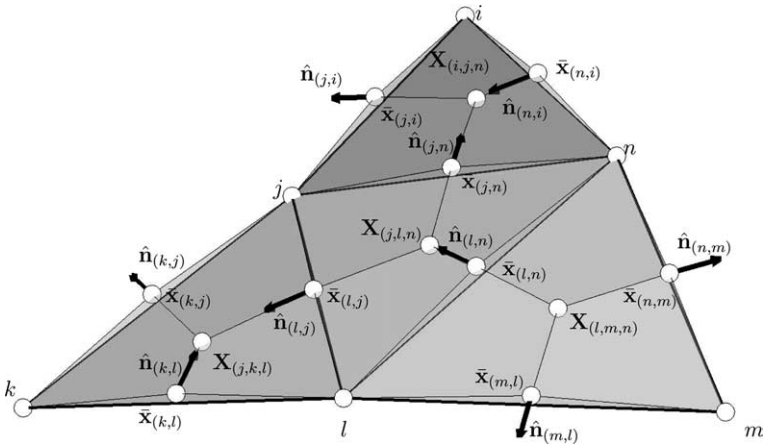

Fig. 2. A representation of four neighboring surface triangles that illustrates the indexing scheme, as well as some relevant geometric quantities (nodes, edge midpoints and normals, and face circumcenters).

$$\bar{\mathbf{x}}_{\mathbf{e}} = \frac{\mathbf{x}_{e_1} + \mathbf{x}_{e_2}}{|\mathbf{x}_{e_1} + \mathbf{x}_{e_2}|}, \quad \hat{\mathbf{n}}_{\mathbf{e}} = \frac{\mathbf{x}_{e_1} \times \mathbf{x}_{e_2}}{|\mathbf{x}_{e_1} \times \mathbf{x}_{e_2}|}, \tag{6}$$

while $\mathbf{X}$ denotes triangle circumcenters, as determined by the equation system

$$\begin{aligned} &[\gamma \mathbf{X}_{\mathbf{c}} - \bar{\mathbf{x}}_{(c_1,c_2)}] \cdot (\mathbf{x}_{c_2} - \mathbf{x}_{c_1}) = 0, \\ &[\gamma \mathbf{X}_{\mathbf{c}} - \bar{\mathbf{x}}_{(c_1,c_3)}] \cdot (\mathbf{x}_{c_3} - \mathbf{x}_{c_1}) = 0, \\ &(\gamma \mathbf{X}_{\mathbf{c}} - \mathbf{x}_{c_1}) \cdot [(\mathbf{x}_{c_2} - \mathbf{x}_{c_1}) \times (\mathbf{x}_{c_3} - \mathbf{x}_{c_1})] = 0, \end{aligned} \tag{7}$$

where γ is determined so as to project $\mathbf{X}_{\mathbf{c}}$ onto the sphere (i.e., to ensure $\mathbf{X}_{\mathbf{c}} \cdot \mathbf{X}_{\mathbf{c}} = 1$). The geodesic lengths of edges and the areas of spherical triangles, denoted, respectively, by ℓ and A, are also important geometric quantities, and are determined by the formulas:

$$\begin{aligned} \ell_{\mathbf{e}} &= \operatorname{acos}(\mathbf{x}_{e_1} \cdot \mathbf{x}_{e_2}), \\ A_{\mathbf{c}} &= \operatorname{acos}\left[\frac{(\mathbf{x}_{c_1} \times \mathbf{x}_{c_2}) \cdot (\mathbf{x}_{c_3} \times \mathbf{x}_{c_2})}{|\mathbf{x}_{c_1} \times \mathbf{x}_{c_2}||\mathbf{x}_{c_3} \times \mathbf{x}_{c_2}|}\right] + \operatorname{acos}\left[\frac{(\mathbf{x}_{c_2} \times \mathbf{x}_{c_3}) \cdot (\mathbf{x}_{c_1} \times \mathbf{x}_{c_3})}{|\mathbf{x}_{c_2} \times \mathbf{x}_{c_3}||\mathbf{x}_{c_1} \times \mathbf{x}_{c_3}|}\right] + \operatorname{acos}\left[\frac{(\mathbf{x}_{c_2} \times \mathbf{x}_{c_1}) \cdot (\mathbf{x}_{c_3} \times \mathbf{x}_{c_1})}{|\mathbf{x}_{c_2} \times \mathbf{x}_{c_1}||\mathbf{x}_{c_3} \times \mathbf{x}_{c_1}|}\right] - \pi. \end{aligned} \tag{8}$$

We now consider the notation for linear matrix operations relating quantities defined over cells and edges, and, in particular, the respective symbols Δ and Δ^{T} are introduced to define a cell-to-edge difference operator and its transpose: i.e.,

$$(\Delta \Phi)_{\mathbf{e}} = \sum_{\mathbf{c}} \delta_{\mathbf{e},\mathbf{c}} \Phi_{\mathbf{c}}, \quad (\Delta^{\mathrm{T}} \lambda)_{\mathbf{c}} = \sum_{\mathbf{e}} \delta_{\mathbf{e},\mathbf{c}} \lambda_{\mathbf{e}}. \tag{9}$$

The sums in Eq. (9) range over all index permutations corresponding to cells or edges of the mesh and the definition of the matrix coefficients,

$$\delta_{\mathbf{e},\mathbf{c}} \equiv \delta_{e_1 c_1}\delta_{e_2 c_2} + \delta_{e_1 c_2}\delta_{e_2 c_3} + \delta_{e_1 c_3}\delta_{e_2 c_1} - \delta_{e_1 c_1}\delta_{e_2 c_3} - \delta_{e_1 c_2}\delta_{e_2 c_1} - \delta_{e_1 c_3}\delta_{e_2 c_2}, \tag{10}$$

is such that, if (c_1, c_2, c_3) and (c_4, c_2, c_1) refer to two adjacent triangles with common edge (c_1, c_2), then the difference of a field across this edge is

$$(\Delta \Phi)_{(c_1,c_2)} = \Phi_{(c_1,c_2,c_3)} - \Phi_{(c_4,c_2,c_1)}$$

(with the minuend being the value on the triangle whose indices are in cyclical order with respect to the edge).

Now, if G is a scalar field that is evaluated at triangle circumcenters and $\mathbf{F}$ is a vector field whose normal component, $F^{\perp} = \hat{\mathbf{n}} \cdot \mathbf{F}$, is evaluated at edge midpoints, then we can approximate the internal edge-values of the normal gradient of G and the cell-values of the horizontal divergence of $\mathbf{F}$ by the respective expressions:

$$\begin{aligned}\hat{\mathbf{n}}\cdot\nabla G &\approx \frac{\Delta G}{|\Delta \mathbf{X}|} = |\Delta\mathbf{X}|_{\mathbf{e}}^{-1}\sum_{\mathbf{c}}\delta_{\mathbf{e},\mathbf{c}}G_{\mathbf{c}},\\ \nabla_{\mathrm{h}}\cdot\mathbf{F} &\approx -\frac{1}{A}\Delta^{\mathrm{T}}[\ell F^{\perp}] = -A_{\mathbf{c}}^{-1}\sum_{\mathbf{e}}\delta_{\mathbf{e},\mathbf{c}}\ell_{\mathbf{e}}F^{\perp}_{\mathbf{e}},\end{aligned} \tag{11}$$

in which $|\Delta\mathbf{X}|_{\mathbf{e}}$ can be identified with the arc length between the circumcenters of the triangles adjacent to $\mathbf{e}$. Boundary edges must usually be handled in special ways for the gradient approximation in Eq. (11), but the appropriate treatment of common boundary conditions is straightforward, and in our notation we will simply absorb any inhomogeneous terms that arise into the forcing terms of Eqs. (1) and (4). In Eq. (11) and in what follows, we also take a few other liberties in order to achieve a more compact notation – for instance, unindexed sums, products, quotients, etc., of fields will be taken to imply $(\Phi_1 \mathrm{Op} \Phi_2)_{\mathbf{c}} = \Phi_{1\mathbf{c}}\mathrm{Op}\Phi_{2\mathbf{c}}$ when the context makes the meaning clear.

The discussion thus far applies fairly generically to the family of orthogonal unstructured grid techniques (e.g., Casulli and Walters [8]), and we recall, for example, that such techniques are first order accurate in the sense that the face midpoints, $\bar{\mathbf{x}}$ (where $\hat{\mathbf{n}}\cdot\nabla G$ is evaluated), do not necessarily coincide with the midpoints between triangle circumcenters, $\mathbf{X}$ (where G is evaluated), except over uniform triangular grids. Other unstructured finite volume methods, such as those used in the coastal model of Chen et al. [9], invoke approximations that may be nominally more accurate than Eq. (11), but the matrix representations of gradients and divergences under these schemes cannot be related by a simple transpose. This property is of fundamental importance to our energy-conserving staggered grid scheme, in which gradient and divergence are the fundamental operations. At the end of this subsection we suggest a simple grid adjustment that may enhance accuracy without compromising the algebraic properties of the scheme.

The grid is staggered in the sense that there is a transformation back and forth between a representation of a vector field $\mathbf{F}$ at triangle circumcenters and the alternative representation of its normal components, $F^{\perp}$, at edges. Because of the differing numbers of degrees of freedom involved, this is not a formally invertible relation, but one can nevertheless define approximations based upon the identities

$$\begin{aligned}F_i &= (\mathbf{F}\cdot\nabla)x_i = \nabla\cdot(x_i\mathbf{F}) - x_i\nabla\cdot\mathbf{F},\\ F^{\perp} &= \mathbf{F}\cdot\frac{\partial\mathbf{x}}{\partial n} = \frac{\partial\mathbf{x}\cdot\mathbf{F}}{\partial n} - \mathbf{x}\cdot\frac{\partial\mathbf{F}}{\partial n},\end{aligned} \tag{12}$$

which discretize to

$$\begin{aligned}\mathbf{F} &\approx \vec{I}F^{\perp} \equiv \frac{\mathbf{X}\Delta^{\mathrm{T}}(\ell F^{\perp}) - \Delta^{\mathrm{T}}(\ell\bar{\mathbf{x}}F^{\perp})}{A},\\ F^{\perp} &\approx \vec{I}^{-1}\cdot\mathbf{F} \equiv \frac{\Delta(\mathbf{X}\cdot\mathbf{F}) - \bar{\mathbf{x}}\cdot\Delta\mathbf{F}}{|\Delta\mathbf{X}|}.\end{aligned} \tag{13}$$

With sums written out explicitly, Eqs. (13) become,

$$\begin{aligned}\mathbf{F}_{\mathbf{c}} &\approx (\vec{I}F^{\perp})_{\mathbf{c}} \equiv \frac{1}{A_{\mathbf{c}}}\sum_{\mathbf{e}}\delta_{\mathbf{e},\mathbf{c}}(\mathbf{X}_{\mathbf{c}} - \bar{\mathbf{x}}_{\mathbf{e}})\ell_{\mathbf{e}}F^{\perp}_{\mathbf{e}},\\ F^{\perp}_{\mathbf{e}} &\approx (\vec{I}^{-1}\cdot\mathbf{F})_{\mathbf{e}} \equiv \frac{1}{|\Delta\mathbf{X}|_{\mathbf{e}}}\sum_{\mathbf{c}}\delta_{\mathbf{e},\mathbf{c}}(\mathbf{X}_{\mathbf{c}} - \bar{\mathbf{x}}_{\mathbf{e}})\cdot\mathbf{F}_{\mathbf{c}},\end{aligned} \tag{14}$$

which implies

$$\begin{aligned}\sum_{\mathbf{e}}\ell_{\mathbf{e}}|\Delta\mathbf{X}|_{\mathbf{e}}F^{\perp}_{\mathbf{e}}(\vec{I}^{-1}\cdot\mathbf{G})_{\mathbf{e}} &= \sum_{\mathbf{e}}\left[\sum_{\mathbf{c}}\delta_{\mathbf{e},\mathbf{c}}(\mathbf{X}_{\mathbf{c}} - \bar{\mathbf{x}}_{\mathbf{e}})\cdot\mathbf{G}_{\mathbf{c}}\right]\ell_{\mathbf{e}}F^{\perp}_{\mathbf{e}} = \sum_{\mathbf{c}}\left[\sum_{\mathbf{e}}\delta_{\mathbf{e},\mathbf{c}}(\mathbf{X}_{\mathbf{c}} - \bar{\mathbf{x}}_{\mathbf{e}})\ell_{\mathbf{e}}F^{\perp}_{\mathbf{e}}\right]\cdot\mathbf{G}_{\mathbf{c}}\\ &= \sum_{\mathbf{c}}A_{\mathbf{c}}\mathbf{G}_{\mathbf{c}}\cdot(\vec{I}F^{\perp})_{\mathbf{c}},\end{aligned} \tag{15}$$

(with $\mathbf{G}$ being another arbitrary vector field over cells) and setting $\mathbf{G} = \mathbf{F}$ gives the following result for the area integrals of vector norms: i.e.,

$$\sum_{\mathbf{c}} A_{\mathbf{c}} \mathbf{F}_{\mathbf{c}} \cdot \mathbf{F}_{\mathbf{c}} \approx \sum_{\mathbf{e}} \ell_{\mathbf{e}} |\Delta \mathbf{X}|_{\mathbf{e}} (F_{\mathbf{e}}^{\perp})^2. \tag{16}$$

Some of the above reasoning steps can be found in the previous analyses of Perot [16], who used a more geometric approach in the flat Cartesian plane. Assuming unit thickness in the $\hat{\mathbf{z}}$ direction, comparisons can be made through the following interchanges of notation: $\ell_{\mathbf{e}} \leftrightarrow A_f$ for edge lengths; $|\Delta \mathbf{X}|_{\mathbf{e}} \leftrightarrow W_f$ for circumcenter to circumcenter distances; $\bar{\mathbf{x}}_{\mathbf{e}} - \mathbf{X}_{\mathbf{c}} \leftrightarrow W_f^{\mathrm{C}} \hat{\mathbf{n}}_f$ for edge midpoint to circumcenter displacements; and $A_{\mathbf{c}} \leftrightarrow V_{\mathrm{c}}$ for cell areas. However, the above approach also sheds further light on the basic analysis, in addition to generalizing it to non-flat surfaces. For instance, Perot explicitly discusses and proves the scheme for approximating cell vectors in terms of their edge-normal components (as per our $\vec{\Gamma}$ operator), but, when projecting the advective and diffusive flux divergences of vector fields from cells to edges (as per our $\vec{\Gamma}^{-1}$ operator), he simply introduces weights of W_f^C / W_f in an apparently arbitrary way. Our analysis provides a rational basis for this step, which is counterintuitive in the sense that it assigns higher weight to the circumcenter that is *farther* from the edge, whereas a naïve linear interpolation would assign higher weight to the *nearer* circumcenter. Also, the basis for the kinetic energy conservation property of the staggered grid discretization will be seen to be a natural consequence of Eq. (15), which can be expressed succinctly as a relation,

$$\vec{\Gamma}^{-1} \cdot \mathbf{F} = \frac{\vec{\Gamma}^{\mathrm{T}} \cdot (A\mathbf{F})}{\ell |\Delta \mathbf{X}|}, \tag{17}$$

between $\vec{\Gamma}^{-1}$ and the matrix transpose of $\vec{\Gamma}$.

Because the deviations of a short spherical arc of length h from planarity are $\mathcal{O}(h^2)$, there is no degradation of the $\mathcal{O}(h)$ accuracy of the gradient and divergence operations of Eq. (11). However, the final discrete momentum equation will depend upon additive and multiplicative combinations of such operations, so it is not immediately obvious how it will be affected by sphericity. The Lagrangian constraint term, $\Lambda \hat{\mathbf{r}}$, in Eq. (4) provides a means of quantifying this effect. When the horizontal momentum dynamics are self-consistently discretizatized, the contribution of the constraint term should vanish, suggesting that the error be quantified in terms of its horizontal projection: i.e., as $\mathcal{O}(\vec{\Gamma}^{-1} \cdot \Lambda \mathbf{X})$. Considering an edge, $\mathbf{e}$, between two triangles, $\mathbf{c}_a$ and $\mathbf{c}_b$, the geometric relationship between midpoints and circumcenters allows us to write,

$$\bar{\mathbf{x}}_{\mathbf{e}} \approx \frac{1}{2}(\mathbf{X}_{\mathbf{c}_a} + \mathbf{X}_{\mathbf{c}_b}) + \frac{\alpha_{\mathbf{e}}}{2}(\mathbf{X}_{\mathbf{c}_b} - \mathbf{X}_{\mathbf{c}_a}) \tag{18}$$

and if we use this in tandem with the identity that $\mathbf{X}_{\mathbf{c}} \cdot \mathbf{X}_{\mathbf{c}} = 1$ for all cells on the sphere, then Eq. (13) gives

$$\left(\vec{\Gamma}^{-1} \cdot \Lambda \mathbf{X}\right)_{\mathbf{e}} = \frac{\Lambda_{\mathbf{c}_b} - \Lambda_{\mathbf{c}_a} - \bar{\mathbf{x}}_{\mathbf{e}} \cdot (\Lambda_{\mathbf{c}_b} \mathbf{X}_{\mathbf{c}_b} - \Lambda_{\mathbf{c}_a} \mathbf{X}_{\mathbf{c}_a})}{|\Delta \mathbf{X}|_{\mathbf{e}}} \approx \frac{(1 - \mathbf{X}_{\mathbf{c}_a} \cdot \mathbf{X}_{\mathbf{c}_b})}{2|\Delta \mathbf{X}|_{\mathbf{e}}} [\Lambda_{\mathbf{c}_b} - \Lambda_{\mathbf{c}_a} - \alpha_{\mathbf{e}}(\Lambda_{\mathbf{c}_a} + \Lambda_{\mathbf{c}_b})]. \tag{19}$$

The significance of the edge midpoint displacement factor, $\alpha_{\mathbf{e}}$, is that it uniformly vanishes for a regular triangular grid in which the edge midpoints coincide with the midpoints between circumcenters. Such an ideal configuration can be realized geometrically in the Cartesian plane, but not on the sphere, except with a handful of Platonic polyhedra. In general, for a non-ideal grid, $\alpha_{\mathbf{e}}$ is $\mathcal{O}(1)$, and the error of Eq. (19) is easily shown to be $\mathcal{O}(|\Delta \mathbf{X}|)$ with the aid of the arc-length formula: i.e.,

$$\mathbf{X}_{\mathbf{c}_a} \cdot \mathbf{X}_{\mathbf{c}_b} \approx \cos |\Delta \mathbf{X}|_{\mathbf{e}} \approx 1 - \frac{1}{2} |\Delta \mathbf{X}|_{\mathbf{e}}^2.$$

Eq. (18) suggests a simple geometric adjustment that can be applied to modestly irregular grids on the sphere or plane, and that would appear to improve the numerical properties of the scheme at no cost. The modification, as it applies to one edge in a flattened geometry, is illustrated in the construction of Fig. 3, and involves the attribution of lateral curvature to the bounding edges between triangular cells. Specifically, the straight edge $\mathbf{e}$ becomes a circular arc whose concave or convex curvature is sufficient to make the midpoint of the arc coincide with the midpoint between the circumcenters of the triangles, $\mathbf{c}_a$ and $\mathbf{c}_b$, that it bounds. Algebraically, the transformation is fully determined by the translation of the midpoint: $\bar{\mathbf{x}}_{\mathbf{e}} \to \frac{1}{2}(\mathbf{X}_{\mathbf{c}_a} + \mathbf{X}_{\mathbf{c}_a})$. The modified discretization retains the same algebraic machinery as the original, except that the length and area fields, ℓ and A, that are used in the divergence approximation and elsewhere are modified as suggested by

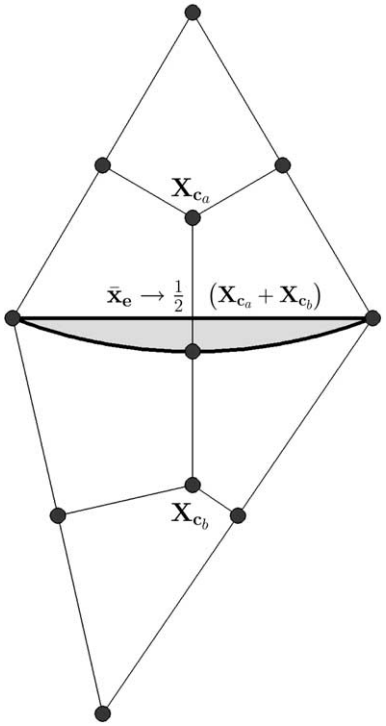

Fig. 3. Adjustment of the shape of edge **e** that is required to make its midpoint coincide with the midpoint between triangle circumcenters $\mathbf{X}_{\mathbf{c}_a}$ and $\mathbf{X}_{\mathbf{c}_b}$.

Fig. 3. Specifically, ℓ becomes the arc length, while the areas of triangles $\mathbf{c}_a$ and $\mathbf{c}_b$ are respectively increased and diminished by the area of the shaded circular segment. For the modified discretization, Eq. (19) suggests that the curvature error is $\mathcal{O}(|\Delta\Lambda||\Delta\mathbf{X}|)$, or $\mathcal{O}(|\nabla\Lambda||\Delta\mathbf{X}|^2)$.

2.4. Vertical discretization and the flux divergence operator

The vertical structure of the ocean will be represented in terms of a number of levels with thickness $\bar{z}_{i-1} - \bar{z}_i$ centered at depth $Z_i = (\bar{z}_{i-1} + \bar{z}_i)/2$, where $\bar{z}_0 = 0$ is the z coordinate of the surface (i.e., where $\sqrt{x^2 + y^2 + z^2} = 1$), and $\bar{z}_{D_\mathbf{c}}$ is the corresponding coordinate at the bottom, which is specified as being $D_\mathbf{c}$ levels deep for cell **c**. The level interface positions $\bar{z}_i$ are constant over the entire globe, meaning that the discrete bathymetry is described by the integral triangle-domain field D, which takes the value $D_\mathbf{c}$ if the averaged ocean bathymetry over triangle **c** falls in the interval $(Z_{D_\mathbf{c}}, Z_{D_\mathbf{c}+1}]$.

We will extend our horizontal indexing scheme for cells and edges in such a way that the values of fields Φ and λ are indexed, respectively, as $\Phi_{\mathbf{c},m}$ and $\lambda_{\mathbf{e},m}$, with $m = 1, 2$, etc., referring to loci at increasing depth in relation to the objects indexed by **c** and **e** in the surface triangulation. Because the topology changes with depth, this requires generalized versions of the horizontal difference operator, Δ, and its transpose, Δ^{T}, which are given by

$$(\Delta\Phi)_{\mathbf{e},m} = \sum_{\mathbf{c}} \delta_{\mathbf{e},\mathbf{c}}\theta_{m,D_\mathbf{c}}\Phi_{\mathbf{c},m}, \quad (\Delta^{\mathrm{T}}\lambda)_{\mathbf{c},m} = \sum_{\mathbf{e}} \delta_{\mathbf{e},\mathbf{c}}\theta_{m,D_\mathbf{c}}\lambda_{\mathbf{e},m}, \tag{20}$$

where $\theta_{m,n}$ is 1 if $m \leqslant n$ and 0 otherwise. This additional factor serves to cancel triangles that exist in the maximal ocean domain without being wetted at level $m > 1$. The results of the previous subsection then apply on each radial level. Because the total non-dimensional ocean depth, $\bar{z}_0 - \bar{z}_{D_\mathbf{c}}$, nowhere exceeds about 0.001, we can, for this application, neglect the variations of ℓ, A, $\Delta\mathbf{X}$, etc., with depth (although this effect is easily added for applications where it is significant).

Although the one-dimensional topology in the vertical direction is very simple, we still define both "untransposed" and "transposed" versions of the vertical difference operator, with Δ_z^{T} applying to differences between quantities defined at adjacent $\bar{z}$ levels, while Δ_z applies to differences between quantities defined at adjacent Z levels – for example,

$$(\Delta_z Z)_m = Z_m - Z_{m+1}, \quad (\Delta_z^{\mathrm{T}} \bar{z})_m = \bar{z}_{m-1} - \bar{z}_m. \tag{21}$$

These definitions shed some additional light on the much more complex discretization of the preceding subsection, and, indeed, the basic approach has been applied directly to three-dimensional meshes for which cell circumcenters and face centroids can be defined (see Zhang et al. [17]). However, for purposes of hydrostatic and other stratified flow applications, the horizontal and vertical dimensions must be decoupled. As in the horizontal discretization, we do not discuss in detail the straightforward implementations of common vertical boundary conditions, and roll-up all inhomogeneous terms into the dynamical forcing.

We now suppose that we are given a non-divergent velocity field as per Eq. (3), with $\mathbf{v} = \mathbf{u} + w\hat{\mathbf{r}}$, for which $u = \mathbf{u} \cdot \hat{\mathbf{n}}$ is prescribed at Z-edges and w is prescribed at $\bar{z}$-cells. This configuration, as well as the overall geometry of the vertical discretization, is depicted in Fig. 4 for a triangular cell, **c**, and its three adjacent edges, **e**, **f**, and **g**. The continuity equation, $\nabla \cdot \mathbf{v}$, and the flux-divergence operator, $\mathscr{L}$, as defined by

$$\mathscr{L}(\mathbf{v}, \kappa, \sigma)\Phi = \mathbf{v} \cdot \nabla\Phi - \mathscr{D}(\kappa, \sigma)\Phi = \nabla \cdot \left(\mathbf{v}\Phi - \kappa \nabla_{\mathrm{h}} \Phi - \hat{\mathbf{r}} \sigma \frac{\partial \Phi}{\partial z} \right), \tag{22}$$

are discretized at Z-cells (i.e., at prism circumcenters) by

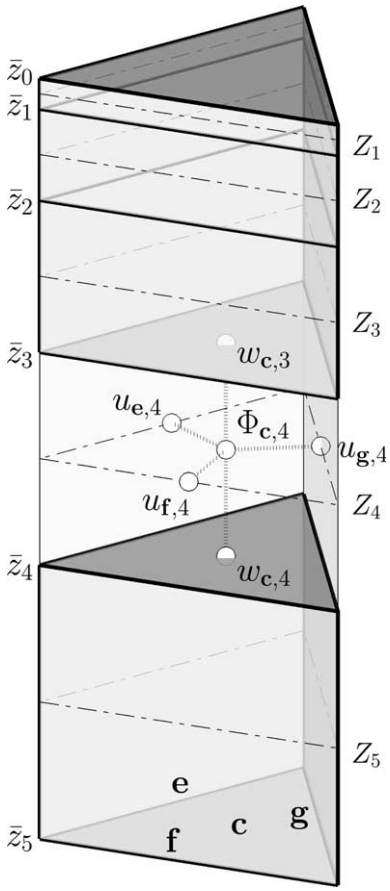

Fig. 4. Radial discretization of a column beneath a cell, **c**, and its adjacent edges, **e**, **f**, and **g**.

$$\mathscr{L}(u,\kappa,\sigma)\Phi \equiv -\frac{1}{A}\Delta^{\mathrm{T}}\left(\ell u\langle\Phi\rangle - \ell\kappa\frac{\Delta\Phi}{|\Delta\mathbf{X}|}\right) - \frac{\Delta_z^{\mathrm{T}}}{\Delta_z^{\mathrm{T}}\bar{z}}\left(w\langle\Phi\rangle_z - \sigma\frac{\Delta_z\Phi}{\Delta_z Z}\right),$$
$$\mathscr{L}(u,0,0)1 = -\frac{1}{A}\Delta^{\mathrm{T}}(\ell u) - \frac{\Delta_z^{\mathrm{T}}w}{\Delta_z^{\mathrm{T}}\bar{z}} = 0, \tag{23}$$

in which Φ is a scalar and the averaging operations are prescribed by

$$\langle\Phi\rangle_{\mathbf{e},m} \equiv \frac{1}{2}(\Phi_{\mathbf{c}_a,m} + \Phi_{\mathbf{c}_b,m}), \quad (\langle\Phi\rangle_z)_{\mathbf{c},m} \equiv \frac{1}{2}(\Phi_{\mathbf{c},m} + \Phi_{\mathbf{c},m+1}) \tag{24}$$

for the respective geometric configurations depicted in Figs. 3 and 4. $\mathscr{L}$ in Eq. (23) is shown depending only upon the horizontal velocity components because w may be diagnosed explicitly from u as

$$w_{\mathbf{c},m} = -\sum_{i=1}^{m}\left[\frac{\Delta_z^{\mathrm{T}}\bar{z}}{A}\Delta^{\mathrm{T}}(\ell u)\right]_{\mathbf{c},m} \tag{25}$$

by means of the discrete continuity equation and the boundary conditions

$$w_{\mathbf{c},0} = w_{\mathbf{c},D_{\mathbf{c}}} = 0. \tag{26}$$

In considering the conservation properties of the discretization, we identify $\mathscr{L}_{\mathrm{h}}$ with the horizontal term of $\mathscr{L}$ on a particular level and form the sum

$$\sum_{\mathbf{c}} A_{\mathbf{c}}\Theta_{\mathbf{c}}(\mathscr{L}_{\mathrm{h}}\Phi)_{\mathbf{c}} = -\sum_{\mathbf{c}}\Theta_{\mathbf{c}}\sum_{\mathbf{e}}\delta_{\mathbf{e},\mathbf{c}}\left[\ell_{\mathbf{e}}u_{\mathbf{e}}\langle\Phi\rangle_{\mathbf{e}} - \frac{\ell_{\mathbf{e}}\kappa_{\mathbf{e}}}{|\Delta\mathbf{X}|_{\mathbf{e}}}(\Delta\Phi)_{\mathbf{e}}\right]$$
$$= \sum_{\mathbf{e}}(\Delta\Theta)_{\mathbf{e}}\left[\ell_{\mathbf{e}}u_{\mathbf{e}}\langle\Phi\rangle_{\mathbf{e}} - \frac{\ell_{\mathbf{e}}\kappa_{\mathbf{e}}}{|\Delta\mathbf{X}|_{\mathbf{e}}}(\Delta\Phi)_{\mathbf{e}}\right], \tag{27}$$

using Θ to denote another arbitrary field. For $\Theta = 1$, it is easily seen that $(\Delta\Theta)_{\mathbf{e}} = 0$ on interior edges and ± 1 on boundary edges so as to make Eq. (27) a simple sum of outward fluxes through boundary edges. For $\Theta = \Phi$, we use the difference of squares,

$$(\Delta\Phi)_{\mathbf{e}}\langle\Phi\rangle_{\mathbf{e}} = \frac{(\Phi_{\mathbf{c}_b} - \Phi_{\mathbf{c}_a})(\Phi_{\mathbf{c}_a} + \Phi_{\mathbf{c}_b})}{2} = \frac{\Phi_{\mathbf{c}_b}^2 - \Phi_{\mathbf{c}_a}^2}{2} = \frac{1}{2}(\Delta\Phi^2)_{\mathbf{e}}, \tag{28}$$

to obtain

$$\sum_{\mathbf{c}} A_{\mathbf{c}}\Phi_{\mathbf{c}}(\mathscr{L}_{\mathrm{h}}\Phi)_{\mathbf{c}} = -\sum_{\mathbf{e}}\sum_{\mathbf{c}}\delta_{\mathbf{e},\mathbf{c}}\Phi_{\mathbf{c}}^2\ell_{\mathbf{e}}u_{\mathbf{e}} + \sum_{\mathbf{e}}\frac{\ell_{\mathbf{e}}\kappa_{\mathbf{e}}}{|\Delta\mathbf{X}|_{\mathbf{e}}}(\Delta\Phi)_{\mathbf{e}}^2 = -\sum_{\mathbf{c}}\Phi_{\mathbf{c}}^2[\Delta^{\mathrm{T}}(\ell u)]_{\mathbf{c}} + \sum_{\mathbf{e}}\frac{\ell_{\mathbf{e}}\kappa_{\mathbf{e}}}{|\Delta\mathbf{X}|_{\mathbf{e}}}(\Delta\Phi)_{\mathbf{e}}^2. \tag{29}$$

If we now define the volume integration operator, $\int$, as

$$\int\Phi \equiv \sum_{\mathbf{c}}\sum_{m=1}^{D_{\mathbf{c}}}\left(\Delta_z^{\mathrm{T}}\bar{z}\right)_m A_{\mathbf{c}}\Phi_{\mathbf{c},m} \tag{30}$$

and go through the steps of adding the corresponding radial terms to the above results, then the following properties of the discretized flux divergence operator can be demonstrated: i.e.,

$$\int\mathscr{L}\Phi = 0,$$
$$\int\Phi\mathscr{L}\Phi = \sum_{\mathbf{e},m}\Delta_z z_m\ell_{\mathbf{e}}\kappa_{\mathbf{e}}\frac{(\Delta\Phi)_{\mathbf{e},m}^2}{|\Delta\mathbf{X}|_{\mathbf{e}}} + \sum_{\mathbf{c},m}A_{\mathbf{c}}\sigma_{\mathbf{c},m}\frac{(\Delta_z\Phi)_{\mathbf{c},m}^2}{\Delta_z Z_m} \geqslant 0, \tag{31}$$

in which we have set the boundary fluxes to zero and made use of the non-divergence condition.

2.5. Time discretization and conservation properties

We now have the tools in place to write down a space-time discretization of the evolution equations in terms of horizontal face-normal velocities, u, as well as prism centred temperature and salinity, T and S: i.e.,

$$\begin{aligned}
&\frac{u^{r+1}-u^r}{\Delta t}+\vec{\Gamma}^{-1}\cdot\left\{[\mathscr{L}(u^r,v_{\mathrm{h}},v_{\mathrm{v}})+4\pi\hat{\mathbf{z}}\times]\vec{\Gamma}u^{r+\frac{1}{2}}-\mathbf{F}_{\mathbf{u}}^r\right\}=-\frac{\Delta p^{r+\frac{1}{2}}}{|\Delta\mathbf{X}|},\\
&\frac{T^{r+1}-T^r}{\Delta t}+\mathscr{L}(u^r,\mu_{\mathrm{h}},\mu_{\mathrm{v}})T^{r+\frac{1}{2}}-F_T^r=0,\\
&\frac{S^{r+1}-S^r}{\Delta t}+\mathscr{L}(u^r,\mu_{\mathrm{h}},\mu_{\mathrm{v}})S^{r+\frac{1}{2}}-F_S^r=0.
\end{aligned}\tag{32}$$

The superscript r specifies the time-level at which a quantity is evaluated, with $\chi^{r+\frac{1}{2}}$ denoting the average $\frac{1}{2}(\chi^r+\chi^{r+1})$ and Δt being the time-step size.

Considering the temperature evolution equation, we have $\int T^{r+1}-\int T^r=\Delta t\int F_T$, which simply expresses the discrete conservation of heat. In the temporal discretizations of u, T and S, the difference of squares gives

$$\frac{(\int T^2)^{r+1}-(\int T^2)^r}{2\Delta t}=-\int T^{r+\frac{1}{2}}\mathscr{L}(u^r,\mu_{\mathrm{h}},\mu_{\mathrm{v}})T^{r+\frac{1}{2}}+\int T^{r+\frac{1}{2}}F_T^r.\tag{33}$$

From Eq. (31), we know that the first term on the RHS will either vanish (for $\mu_{\mathrm{h}}=\mu_{\mathrm{v}}=0$) or remain strictly negative definite if either dissipation coefficient is positive. Hence, in the absence of any inhomogeneous forcing (i.e., $F_T=0$), the discrete integral $\int T^2$ will be strictly conserved or dissipated, which is a known desirable feature of centred-difference finite-volume advection/diffusion schemes (see Arakawa [28]). Naturally, the same is true for the evolution of salinity, S, and, because of the special relationship between $\vec{\Gamma}^{-1}$ and $\vec{\Gamma}^{\mathrm{T}}$ (Eq. (17)), we can demonstrate a relation similar to Eq. (33) for u. Multiplying the momentum evolution equation by $\ell\Delta_z^{\mathrm{T}}\bar{z}|\Delta\mathbf{X}|u^{r+\frac{1}{2}}$ and summing over all edges, we use Eq. (15) to obtain that,

$$\frac{K^{r+1}-K^r}{\Delta t}=-\int\mathbf{U}^{r+\frac{1}{2}}\cdot\mathscr{L}(u^r,v_{\mathrm{h}},v_{\mathrm{v}})\mathbf{U}^{r+\frac{1}{2}}+\int\mathbf{U}^{r+\frac{1}{2}}\cdot\mathbf{F}_{\mathbf{u}}^r+P_*^{r+\frac{1}{2}},\tag{34}$$

in which $\mathbf{U}\equiv\vec{\Gamma}u$, $P_*^{r+\frac{1}{2}}$ is a baroclinic energy conversion term (see below), and

$$K^r\equiv\frac{1}{2}\sum_{\mathbf{e},m}\ell_{\mathbf{e}}|\Delta\mathbf{X}|_{\mathbf{e}}\left(\Delta_z^{\mathrm{T}}\bar{z}\right)_m\left(u_{\mathbf{e},m}^r\right)^2\approx\frac{1}{2}\int|\mathbf{U}^r|^2,\tag{35}$$

where we have employed Eq. (16) to demonstrate that the scalar K^r approximates the total kinetic energy. The Coriolis term does not influence Eq. (34) because of the identity $\mathbf{U}\cdot(\hat{\mathbf{z}}\times\mathbf{U})=0$. Our generalization of Perot's analysis makes clear how one can treat such dynamical terms, as well as boundary conditions and momentum forcing, in a local Cartesian 3-space affixed to a prism, while maintaining the crucial energy budget in the velocity field, which is discretized in terms of normal velocities at its horizontal edges.

The baroclinic energy conversion term, P_*, is defined, and can be further manipulated, as follows:

$$P_*\equiv-\sum_{\mathbf{e},m}\left(\Delta_z^{\mathrm{T}}\bar{z}\right)_m(\ell u\Delta p)_{\mathbf{e},m}=\int\frac{p}{A}\Delta^{\mathrm{T}}(\ell u)=\sum_{\mathbf{c},m}(wA\Delta_z p)_{\mathbf{c},m},\tag{36}$$

and if we discretize the hydrostatic balance relation as

$$\Delta_z p=-\langle\rho\Delta_z^{\mathrm{T}}\bar{z}\rangle_z,\tag{37}$$

it can be shown through additional algebra that Eq. (36) is equivalent to

$$P_*=-\int\langle w\rangle_z\rho=-\int Z[\mathscr{L}(u,\mu_{\mathrm{h}},\mu_{\mathrm{v}})\rho-F_\rho],\tag{38}$$

in which F_ρ is an appropriate inhomogeneous forcing on the density field. The initial RHS terms of Eqs. (34) and (38) demonstrate the appropriate discrete kinetic-potential energy flux conservation law for the rigid-lid Bryan–Cox–Semtner model (see Dukowicz and Smith [29]).

On the topic of the energy budget, we could, in fact, obtain an even stronger conservation principle if we were to replace either the thermal or the saline conservation law in the discrete equations (32) with a discrete buoyancy equation of the form

$$\frac{\rho^{r+1}-\rho^{r}}{\Delta t}+\mathscr{L}\left(u^{r+\frac{1}{2}},\mu_{\mathrm{h}},\mu_{\mathrm{v}}\right)\rho^{r+\frac{1}{2}}-F_{\rho}^{r}=0. \tag{39}$$

Under these conditions, Eq. (38) substituted into Eq. (34) would enable us to define a discrete total (kinetic plus potential) energy as:

$$E^{r}=K^{r}+\int Z\rho^{r}. \tag{40}$$

However, among other modest complications, this would entail evaluating the advecting velocity in Eq. (39) at time level $r+\frac{1}{2}$, and thus solving nonlinear equation systems to determine fields at time level $r+1$ from those at level r. Another potential improvement that could be achieved at the expense of increased storage requirements relates to the formal temporal accuracy of the scheme, which would become second-order if conservation were imposed at $r+\frac{1}{2}$ time levels (e.g., on $K^{r+\frac{1}{2}}$ as opposed to K^{r}), with a leapfrog-like time-stepping scheme of the form

$$\frac{T^{r+\frac{1}{2}}-T^{r-\frac{1}{2}}}{\Delta t}+\mathscr{L}(u^{r},\mu_{\mathrm{h}},\mu_{\mathrm{v}})\left(\frac{T^{r+\frac{1}{2}}+T^{r-\frac{1}{2}}}{2}\right)-F_{T}^{r}=0 \tag{41}$$

for determining temperature (and analogously for salinity and momentum). In this work, we restrict ourselves to the analysis of the cheapest, first-order space-time discretization with kinetic-only energy conservation, understanding that further refinements are possible if a demanding application requires them.

Before leaving the topic of discrete invariants, we consider the momentum conservation properties of the discretization. Perot [16] showed that this quantity also is conserved for the Navier–Stokes equations on the flat plane, but the result does not carry over to the sphere. Considering one radial level only (with unit depth), a component of total momentum must be defined with respect to a coordinate basis vector, $\mathbf{q}_{\mathbf{c}}$, that varies from cell-to-cell: i.e.,

$$M_{(q)}\equiv\sum_{\mathbf{c}}A_{\mathbf{c}}\mathbf{q}_{\mathbf{c}}\cdot\mathbf{U}_{\mathbf{c}}=\sum_{\mathbf{c}}A_{\mathbf{c}}\mathbf{q}_{\mathbf{c}}\cdot(\vec{\Gamma}u)_{\mathbf{c}}=\sum_{\mathbf{e}}\ell_{\mathbf{e}}|\Delta\mathbf{X}|_{\mathbf{e}}u_{\mathbf{e}}(\vec{\Gamma}^{-1}\cdot\mathbf{q})_{\mathbf{e}}. \tag{42}$$

In tandem with the discrete momentum evolution equation in (32), this gives

$$\begin{aligned}\frac{M_{(q)}^{r+1}-M_{(q)}^{r}}{\Delta t}&=-\sum_{\mathbf{e}}\ell_{\mathbf{e}}|\Delta\mathbf{X}|_{\mathbf{e}}\left(\vec{\Gamma}^{-1}\cdot\mathbf{q}\right)_{\mathbf{e}}\left(\vec{\Gamma}^{-1}\cdot\mathscr{L}_{\mathrm{h}}\mathbf{U}^{r+\frac{1}{2}}+\frac{\Delta p^{r+\frac{1}{2}}}{|\Delta\mathbf{X}|}\right)_{\mathbf{e}}+\cdots\\&=\sum_{\mathbf{c}}A_{\mathbf{c}}\left(\vec{\Gamma}\vec{\Gamma}^{-1}\cdot\mathbf{q}\right)_{\mathbf{c}}\cdot\mathscr{L}_{\mathrm{h}}\mathbf{U}^{r+\frac{1}{2}}+\sum_{\mathbf{c}}p_{\mathbf{c}}^{r+\frac{1}{2}}\left[\Delta^{\mathrm{T}}(\ell\vec{\Gamma}^{-1}\cdot\mathbf{q})\right]_{\mathbf{c}}+\cdots\end{aligned} \tag{43}$$

(with source terms left out). Eq. (43) shows that the $\mathbf{q}$-component of momentum will be discretely conserved only if the following geometric conditions hold:

$$[\Delta(\vec{\Gamma}\vec{\Gamma}^{-1}\cdot\mathbf{q})]_{\mathbf{e}}=[\Delta^{\mathrm{T}}(\ell\vec{\Gamma}^{-1}\cdot\mathbf{q})]_{\mathbf{c}}=0, \tag{44}$$

in which the first condition is a consequence of Eq. (27) with $\Theta\leftarrow\vec{\Gamma}\vec{\Gamma}^{-1}\cdot\mathbf{q}$. For $\mathbf{q}$ constant on the flat plane, it is easily shown that $\vec{\Gamma}^{-1}\cdot\mathbf{q}=\hat{\mathbf{n}}\cdot\mathbf{q}$ and the conditions (44) are fortuitously satisfied. This ceases to be the case on the sphere, where the quantities vanish only to $\mathscr{O}(|\Delta\mathbf{X}|)$, except perhaps for "special" combinations of grid and basis vector.

In actually integrating the evolution equation (32) over a time step, we first advance the temperature and salinity fields by solving for T^{r+1} and S^{r+1}: i.e., for temperature

$$\left[1+\frac{\Delta t}{2}\mathscr{L}(u^{r},\mu_{\mathrm{h}},\mu_{\mathrm{v}})\right]T^{r+1}=\left[1-\frac{\Delta t}{2}\mathscr{L}(u^{r},\mu_{\mathrm{h}},\mu_{\mathrm{v}})\right]T^{r}+\Delta tF_{T}^{r}, \tag{45}$$

and analogously for salinity. The linear equation system (45) is non-symmetric for $u^{r}\neq 0$, and solving for T^{r+1} requires a generalization of commonly employed conjugate-gradient type algorithms for sparse, symmetric matrix inversion. We use a generalized minimum residual (GMRES) algorithm that was implemented by CERFACS [20], and that is based on the projection of residuals onto subspaces of the Krylov space using

an Arnoldi–Lanczos procedure. With $T^{r+\frac{1}{2}} = \frac{1}{2}(T^r + T^{r+1})$ and $S^{r+\frac{1}{2}} = \frac{1}{2}(S^r + S^{r+1})$ determined, we can use the discrete hydrostatic relation (37) and the equation of state to determine the hydrostatic pressure variation, $p_{\mathrm{h}}^{r+\frac{1}{2}}$. However, because of the vertical boundary conditions, the total pressure, $p^{r+\frac{1}{2}} = \frac{1}{2}(p_s^r + p_s^{r+1}) + p_{\mathrm{h}}^{r+\frac{1}{2}}$, depends also on a surface pressure field, p_s, which is codetermined with lateral velocity, u, at time-level r in such a way as to enforce the vanishing bottom normal velocity condition ($w_{D_\xi}^r = 0$).

As is generally the case in both rigid-lid and free surface ocean models, the evolution equation for horizontal velocity is coupled to an unknown surface field by the bottom boundary condition. In our scheme, the resulting linear equation system that can be written schematically as follows:

$$\left[\mathscr{D}(0) + \frac{\Delta t}{2}\mathscr{D}\left(\frac{2}{\Delta t}\right)\mathscr{P}^r\right]\begin{bmatrix} u^{r+1} \\ p_s^{r+1}\end{bmatrix} = \mathscr{D}\left(\frac{2}{\Delta t}\right)\left\{\left[\mathscr{D}(0) - \frac{\Delta t}{2}\mathscr{P}^r\right]\begin{bmatrix} u^r \\ p_s^r\end{bmatrix} + \Delta t\begin{bmatrix} \vec{\Gamma}^{-1}\cdot\mathbf{F}_{\mathbf{u}}^r - \frac{\Delta p_h^{r+\frac{1}{2}}}{|\Delta\mathbf{x}|} \\ 0\end{bmatrix}\right\}, \tag{46}$$

where

$$\mathscr{D}(\alpha)\begin{bmatrix}\lambda \\ \Phi\end{bmatrix} \equiv \left[\begin{array}{c|c} \lambda & 0 \\ \hline \alpha\sum_m \left[\Delta_z^{\mathrm{T}}\bar{z}\Delta^{\mathrm{T}}(\ell\lambda)\right]_m & 0\end{array}\right] = \left[\begin{array}{c|c} 1 & 0 \\ \hline \alpha\sum_m \{\Delta_z^{\mathrm{T}}\bar{z}\Delta^{\mathrm{T}}[\ell\cdots]\}_m & 0\end{array}\right]\begin{bmatrix}\lambda \\ \Phi\end{bmatrix}, \tag{47}$$

and, similarly,

$$\mathscr{P}^u \equiv \left[\begin{array}{c|c} \vec{\Gamma}^{-1}\cdot\{[\mathscr{L}(u^r, v_h, v_v) + 4\pi\hat{\mathbf{z}}\times]\vec{\Gamma}\cdots\} & \frac{\Delta}{|\Delta\mathbf{x}|} \\ \hline 0 & 0\end{array}\right]. \tag{48}$$

The GMRES algorithm is used once again to iteratively solve for u^{r+1} and p_s^{r+1} (which closes the discrete dynamics, apart from the determination of the mixing coefficients, $\nu_{h,v}$ and $\mu_{\mathrm{h,v}}$, which is discussed in the following subsection). Because the iterative solution procedure simultaneously determines horizontal velocity and surface pressure, our approach differs from an implicit pressure-projection scheme for incompressible CFD (e.g., Löhner and Yang [30]), which would first "predict" an intermediate (and generally divergent) velocity field, $\tilde{u}$, through the momentum equation, and then determine the pressure field that "corrects" away the divergent component. This does not maintain kinetic energy conservation (see the discussion of Mahesh et al. [31]). Ocean models that decouple the barotropic and baroclinic components of the flow are based on an analogous predictor-corrector strategy, whereas in our scheme, the "prediction" and "correction" are subsumed into the rational iteration procedure. In coastal modeling, Casulli and Walters [8] and Zhang et al. [11], following the earlier work of Casulli and Cheng [32], also simultaneously determine surface height/pressure and horizontal momentum, but these authors treat the advective term explicitly, which splits the algebraic problem into simpler SPD systems, but which once again destroys the energy conservation property. Of course, in our scheme, the detailed validity of dynamical constraints depends upon the tolerance used in the iterative solution procedure, which we analyze in tests described in Section 3.1 below.

2.6. Mixing parameterization

The choice of mixing scheme for representing underresolved processes is a major open issue in ocean modeling, and for purposes of this study we will simply illustrate how one frequently used set of assumptions fit into our methodology, and adopt these consistently throughout. A common rule of thumb for specifying the horizontal mixing essentially entails utilizing as little dissipation as needed to achieve numerical stability (see Bryan et al. [33]). To cite an example that involves variable grid resolution over the globe, we mention the analyses of Murray and Reason [34], which highly resolve the South Indian Ocean and coarsely resolve the rest of the world oceans. Strictly speaking, our own methodology is more-or-less unconditionally stable against any unbounded growth in numerical "noise," but simulations become unphysical if we run too far outside the parameter regime prescribed by stability criteria for explicit methods. For the 1-D advection-diffusion problem, it can be shown that if the dissipation is less than $\frac{1}{2}U\ell$ (with U the advection velocity and ℓ the grid spacing), the discrete solution can manifest an algebraic instability (e.g., Clancy [35]). In practice, acceptable solutions can be achieved using a horizontal dissipation coefficient as small as $U_*\ell$, where the "grid velocity"

constant U_* is on the order of 1% of the maximum advecting velocity. Because the momentum equation has more complex dynamics than the thermal and saline advection-diffusion equations, additional instabilities may also arise, and in particular we must ensure that Munk diffusive boundary layers will be thick enough to be resolved by the grid (see Bryan et al. [33]). The required values of ν_h and μ_h are as follows:

$$\nu_{\mathrm{h}} = \min\left\{U_*\ell, 4\pi\cos\theta\left(\frac{\sqrt{3}\ell}{\pi}\right)^3\right\}, \quad \mu_{\mathrm{h}} = U_*\ell, \tag{49}$$

in which θ is the latitude. We do not need to worry about the upper bounds on the dissipation coefficients because of the implicit time discretization.

For vertical dissipation, we utilize the parameterization of Pacanowski and Philander [36], which is given by

$$\nu_{\mathrm{v}} = \frac{\nu_0}{(1+5Ri)^2} + \nu_b, \quad \mu_{\mathrm{v}} = \frac{\nu_{\mathrm{v}}}{(1+5Ri)} + \mu_b, \tag{50}$$

where ν_0, ν_b, and μ_b are constants and the Richardson number at triangular prism faces is computed as

$$Ri = \max\left\{\frac{\Delta_z Z \Delta_z \rho}{|\Delta_z \mathbf{U}_*|^2 + \epsilon}, 0\right\} \tag{51}$$

(ϵ in the denominator being a small number introduced to avoid divisions by zero). With our implicit temporal discretization and large ν_0, Eq. (50) effectively includes a convective parameterization, as convectively unstable gradients with $\Delta_z\rho < 0$ will be strongly dissipated.

3. Numerical tests

3.1. Kinetic energy conserving dynamics

The first tests that will be described are designed to verify the conservation properties of the momentum discretization, and establish the dependence of numerical errors and iteration counts on the GMRES tolerance parameter, ϵ_{tol}. If a trivial equation of state with $\rho_{\mathrm{T}} = \rho_{\mathrm{S}} \equiv 0$ is prescribed, then there is no coupling between the momentum, temperature and/or salinity dynamics and the baroclinic energy conversion term P_*, in Eq. (34) becomes irrelevant. If, moreover, there is no dissipation (i.e., $\nu_{\mathrm{h}} = \nu_{\mathrm{v}} = 0$), no forcing, and no boundary momentum flux, then the remaining terms also vanish and an exact solution of the discrete momentum equation should yield $K^r = K^0$ for arbitrary time level r. On the basis of this we can define a measure of relative error in total kinetic energy as

$$\epsilon_K \equiv \frac{|K^r - K^0|}{K^0}. \tag{52}$$

Another measure of error can be related to the bottom normal velocity predicted by integrating the divergence down through the pressure column, which should be identically 0. The quantity

$$\epsilon_w \equiv \sqrt{\frac{\sum_{\mathbf{c}}(D_{\mathbf{c}}+1)w_{D_{\mathbf{c}}}^2}{\sum_{\mathbf{c},m} w_{\mathbf{c},m}^2}} \tag{53}$$

is hence a measure of the errors in the surface pressure and horizontal divergence though the water columns at all triangles in the ocean domain. In order to prevent such errors from impacting upon the global conservation properties of the advection-diffusion operator $\mathscr{L}$, $w_{D_{\mathbf{c}}} = 0$ is still summarily imposed at the ocean bottom, which cancels all local "gains" and "losses" over a column in the lowermost cell.

The model has been run under the above discussed energy conserving conditions, using seven variable-thickness vertical levels (spanning $z_m = 0$, 25, 50, 100, 200, 400, 800, and 1600 m) and a simple horizontal grid with relatively coarse resolution (about 2°). In this configuration we integrated five cases in which ϵ_{tol} was set to the respective values 10^{-3}, 10^{-4}, 10^{-5}, 10^{-6}, and 10^{-7} for 1000 steps totaling 10 nondimensional units of simulation time per case (this being 10 days of physical time at a time step of about 15 min). An identical

initial condition was applied in each case, with the u^0 and p_s^0 fields having been created over an earlier 30 day forced and dissipative simulation. In this setup, the ocean domain was spun up from rest by a surface wind stress that was applied as an intense retrograde equatorial jet. This resulted in a flow pattern that had features in common with the oceanic circulation, but that was contrived to be unrealistically intense in order to facilitate short test simulations that could exhibit nonlinear dynamics at large scales.

Although the initial field, u^0, is qualitatively "physical," simulations with no dissipation invariably develop into unphysical states, so we will not discuss the dynamics directly. The reader's attention is directed instead to Fig. 5, which shows the number of iterations per step used over the 10 days of the five respective cases. This gives an idea of how the computational cost increases as ϵ_{tol} decreases, and it can be inferred from the logarithmic plot that the iteration counts scale approximately with $1/\sqrt{\epsilon_{\text{tol}}}$. Obviously, the cost of using extremely small tolerances becomes prohibitive, but it will be shown in what follows that one need not, for practical purposes, go below about 10^{-4}, except to demonstrate the properties of the numerical scheme. All of the cases except the one with the loosest GMRES tolerance ($\epsilon_{\text{tol}} = 10^{-3}$) have, by about $t = 5$, fallen into quasi-steady regimes in which their iteration counts per step fluctuate about stable levels. Examination of the corresponding fields verifies that they are characterized by unphysical grid-scale artefacts, but, in contrast with other numerical schemes, this "noise" does not trigger the unbounded growth of velocity components, and their dynamics are reproduced consistently at different ϵ_{tol} values. The sole exception, the case with $\epsilon_{\text{tol}} = 10^{-3}$, begins to develop anomalous large-scale currents at high latitudes, which suggests the onset of a runaway instability.

Fig. 6 shows semi-logarithmic plots of the kinetic energy conservation and bottom velocity errors, ϵ_K and ϵ_w, over the 10 days of our 5 cases. As would be expected, these errors are attenuated as ϵ_{tol} decreases, with the dependence appearing to be approximately linear in both cases. There are some fluctuations in the ϵ_K curve, but the results nevertheless show how the energy error, as well as the bottom velocity error, are being reduced essentially to the level of numerical roundoff when ϵ_{tol} is set very small. Fig. 6 also shows further evidence that the $\epsilon_{\text{tol}} = 10^{-3}$ case produces unacceptable results. By the end of the 10 days, there is an almost 100% discrepancy in kinetic energy, while the bottom velocity error appears to exhibit continuing systematic growth. In contrast, all of the other error curves are approaching saturation, with the next largest kinetic energy error, corresponding to the $\epsilon_{\text{tol}} = 10^{-4}$ case, being only about 2%. Further, lengthier simulations that included dissipation, forcing, and baroclinicity have established that this tolerance level in the momentum solution is sufficient to achieve robust and stable dynamics under a wide variety of grid resolutions, flow patterns and flow intensities. The GMRES tolerance for solving the implicit heat and salinity transport equations must be set at a lower level – about 10^{-6} – in order to avoid occasional numerical problems in baroclinic simulations. However, the iterative matrix inversions for the scalar equations also converge much more rapidly, and in all only a handful of solver iterations per step are required to perform reasonable integrations. As is evident

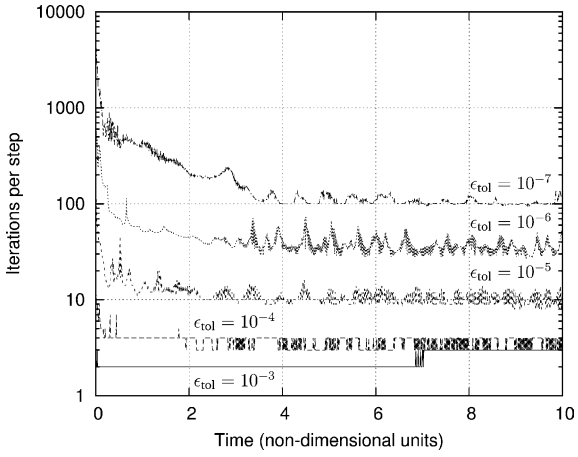

Fig. 5. Solver iteration counts per step for 1000 steps of 5 kinetic-energy conserving integrations with different solver tolerances.

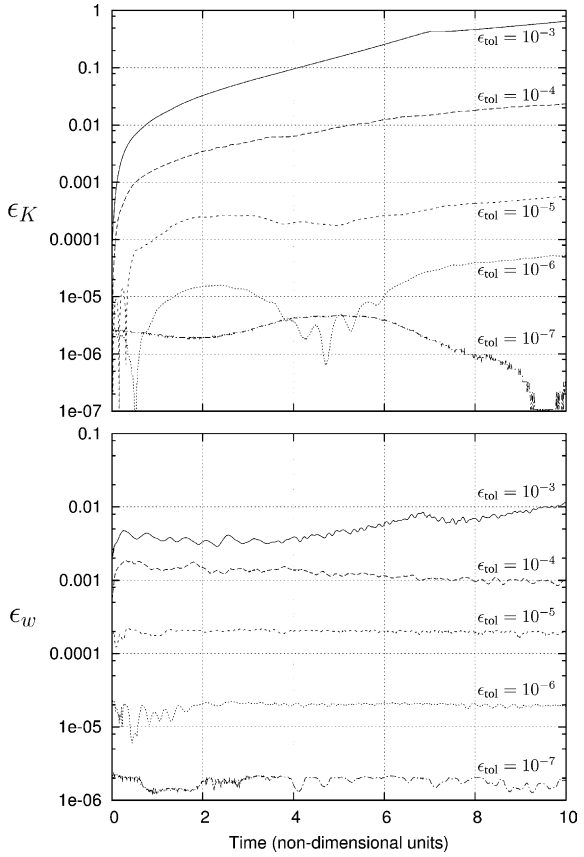

Fig. 6. Errors in kinetic energy ($\epsilon_K = |K^r - K^0|/K^0$) and bottom velocity ($\epsilon_w$) vs. time step for 5 integrations with different solver tolerances.

from Figs. 5 and 6, transients arising from sudden changes in simulation conditions place a temporary load on the solver.

3.2. Density front adjustment

The next tests that will be discussed relate to the geostrophic adjustment of an initial state and to the breakdown of the ensuing flow pattern through the development of baroclinic instability. Such phenomena are of crucial importance in atmosphere/ocean dynamics, although in the ocean their spatial extent is usually prescribed by the thermocline and the Rossby radius of deformation, which are quite small in relation to the respective vertical and horizontal extents of the flow domain. One of the potential advantages of our numerical methodology is in its capacity to selectively refine the global grid in regions where "eddy permitting" dynamics are known to be required. However, realistic simulations of the thermocline circulation, which is continuously forced by surface heat, buoyancy, and momentum fluxes, are very complex dynamically, and hence not a good context in which to discern how well the numerical methodology is resolving basic fluid dynamical processes.

In order to perform a quantitatively interpretable experiment that exhibits the dynamics of geostrophic adjustment and baroclinic instability, we considered the problem of density front adjustment on a global scale, in the geometry of the real oceans. This unforced, dissipative process has previously been studied through experiments and numerical simulations in simple rotating geometries (see, e.g., Hallworth et al. [37] and Stegner et al. [38]) in which a confined bolus of dense fluid is suddenly released and allowed to slump into a reservoir of lighter fluid. Such dynamics are of direct relevance to the atmosphere and oceans, but not on the global scale. However, if one imagines a vast idealization of the atmosphere-ocean system in which an isolated

"parcel" of solar energy has somehow heated up an equatorial band, then the global flow of thermal energy can be abstracted in terms of cold, dense fluid slumping back from the poles to the equator. Quite interestingly, we will see that, even without any thermal or wind-stress forcing, some of the gross features of the ocean circulation are reasonably represented in the temporary flow pattern that emerges during geostrophic adjustment and subsequent baroclinic instability. What is significant from our perspective, is the fact of this being an initial value problem with a well-defined energy budget in which there are no sources or sinks apart from dissipation.

The elements of the simulation that are specified a priori are the equation of state, for which we assume a simple linear form with constant thermal and vanishing saline expansion coefficient (i.e., $\rho/\rho_0 = 1 - 2.5^{-4^\circ}\ \mathrm{C}^{-1}\mathrm{T}$), and the initial temperature field, for which we assume the profile

$$T_0 = \begin{cases} 5\ ^\circ\mathrm{C} & \text{if } |\lambda| \geqslant 40^\circ, \\ 5\ ^\circ\mathrm{C} + \frac{25\ ^\circ\mathrm{C}}{2}\left[1 + \cos\left(\frac{|\lambda| - 20^\circ}{20^\circ}\right)\right] & \text{if } |\lambda| < 40^\circ \text{ and } |\lambda| > 20^\circ, , \\ 30\ ^\circ\mathrm{C} & \text{if } |\lambda| \leqslant 20^\circ, \end{cases} \tag{54}$$

which is independent of depth and bathymetry, depending solely on the latitude, λ. Because there is no thermocline in this toy model, we simply discretize the upper 5 km of the ocean with 10 layers of equal thickness. The values used for the dissipation parameters are $U_* = 6$ cm/s, $\nu_b = 1\ \mathrm{cm}^2/\mathrm{s}$, $\nu_0 = 49\ \mathrm{cm}^2/\mathrm{s}$, and $\mu_b = 0.1\ \mathrm{cm}^2/\mathrm{s}$. For these particular values, the system reaches a new quiescent state with stable density distribution after approximately 2 years. Over this period, the velocity–temperature dynamics progress through a sequence of stages that are well understood, and whose signatures can be seen in the time series in Fig. 7, which illustrates the evolution of kinetic, potential, and total energy deviations, as diagnosed from the model fields (and scaled by a nominal potential energy). A logarithmic time scale is used because there are three successive stages whose respective temporal extents differ by an order of magnitude.

The initial thermal/density front is not in geostrophic balance with the zero velocity field, so the first stage of evolution, which takes place over 2–3 days, is the adjustment to balance. There is a distinctive sequence of pulses in which potential and kinetic energy are inter-converted at about 1 day intervals. This is consistent, at mid-latitudes, with the "half pendulum day" (i.e., $\pi/|\Omega_0 \sin\theta|$), which is the characteristic period of inertial oscillation. "Noise" with this period is a common artefact in numerical simulations of baroclinic phenomena, signaling a departure from geostrophic balance in the numerical solution (see, e.g., Polavarapu and Peltier [39] and Yamazaki and Peltier [40]). However, some applications demand the resolution of *bona fide* inertial-type oscillations, and experimental and numerical studies of collapsing density fronts on the rotating *f*-plane have, in particular, shown the initial front exhibiting a number of intense pulsations at the inertial oscillation frequency before adjusting to cyclo-geostrophic balance (see [37,38]). The time series of Fig. 7 show clear evidence that strong inertial oscillations are in play during the first few days of simulation time, when they are expected to occur on physical grounds, but no evidence of significant anomalous oscillations in the later

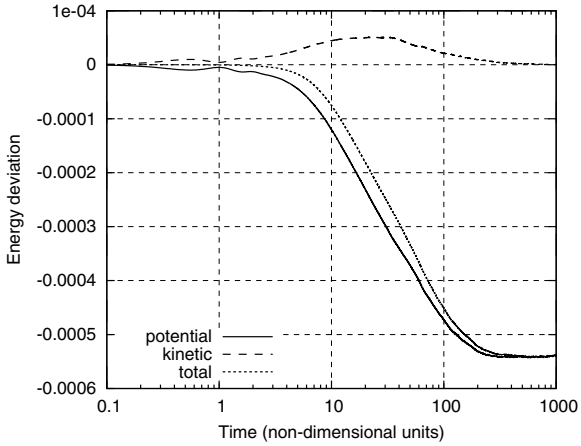

Fig. 7. Evolution of potential, kinetic, and total energies over 1000 days of the collapsing density front simulation.

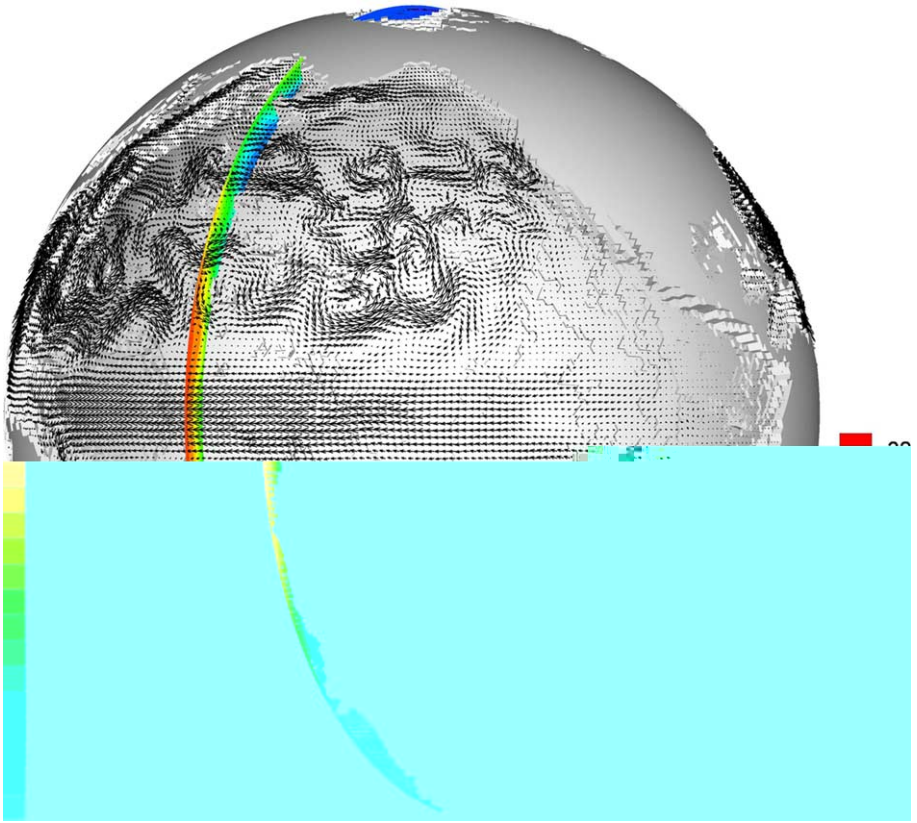

Fig. 8. Temperature field slice and near-surface velocity vector field in the Pacific basin after 100 days of the collapsing density front simulation.

dynamics. This suggests that the representation of geostrophic balance by the numerical structure is physically reasonable. The energetics are also appropriate, with the total (kinetic plus potential) energy being very well conserved in the initial stage of the dynamics, and then monotonically depleted in the later, dissipative stages.

By design, the geostrophic currents that arise from the adjustment of our particular density front are baroclinically unstable, which triggers a secondary, irreversible conversion of potential energy to kinetic energy that is lost to viscous dissipation. The second stage of evolution reflected in our time series corresponds to the initial growth of small-scale baroclinic disturbances, which progresses over about 20 days and then saturates. The third stage, which takes up the balance of the multi-year simulation, is marked by the gradual decay of the kinetic energy due to dissipation. The overall mechanism that is in play is illustrated in Fig. 8, which shows the near-surface velocity vector field in the Pacific basin at 100 days, along with a slice through the temperature field through the 0–180° longitude line (the radial scale in the diagram is exaggerated for clarity). By this point, the potential energy in the initial state has mostly been liberated, which is evident in the fact that cold and warm waters have been extensively redistributed near the bottom and surface, respectively, creating a global stably stratified configuration. The kinetic energy is manifested in the form of a relatively stable equatorial easterly jet and a complementary pair of intense, unstable streams that are deflected into the two hemispheres by western boundaries and/or topography. These deflected currents are breaking down into cyclones and anti-cyclones at smaller scales that are more susceptible to dissipation. The basic pattern is repeated in the other ocean basins (not shown) and is broadly suggestive of the real ocean circulation, although the ''boundary currents'' in this simple experiment are highly distorted and are extremely exaggerated in extent.

Before leaving this subsection, we briefly examine the dynamics of a small portion of the swirling current in the north Pacific basin. Fig. 9 shows the temperature field and the direction of the horizontal current at the $m = 2$ level at the following four times: 100 days (frame a); 104.5 days (frame b); 106.5 days (frame c); and 108.5 days (frame d). Over this period we see the thermal front shedding both a warm core ring and a cold

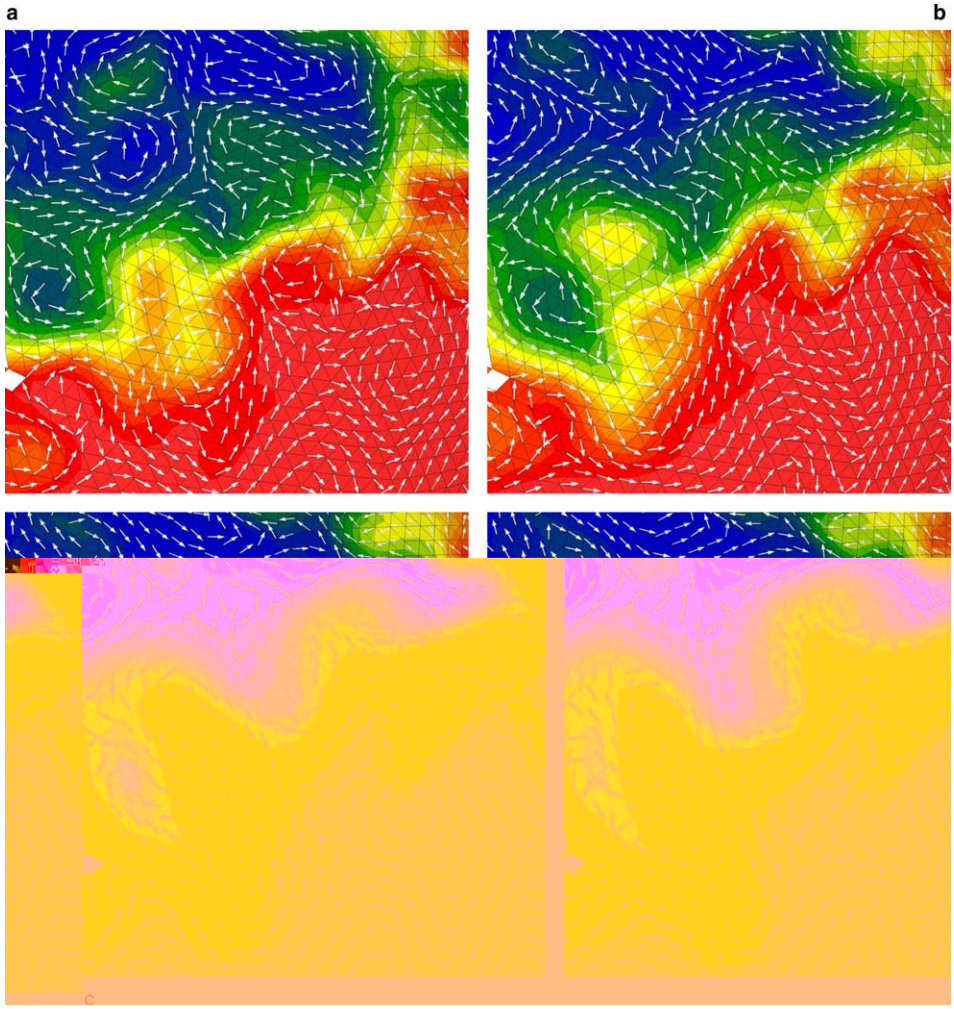

Fig. 9. Close up showing the contoured temperature field and velocity direction at Z-level $m = 2$ in a region of the baroclinically unstable front at 4 times: $t = 100$ days (a), 104.5 days (b), 106.5 days (c), and 108.5 days (d).

core ring consistently with the well-known phenomenology of baroclinic instability in geostrophic ocean currents (see, e.g., Bush et al. [41,42]). The correlation between the current direction and the thermal gradient is characteristic of a geostrophically balanced flow, which is the norm in most regions of the ocean, the exceptions being coastal and equatorial regions, where ageostrophic dynamics can be significant.

3.3. Realistic ocean simulations

The final set of results that we will employ herein for demonstration purposes relate to the ocean circulation forced by realistic climatological data describing the temperature and salinity distributions (Levitus [43]) and the surface wind stress (Hellerman and Rosenstein [44]). This is a very common scenario and can be regarded as a proxy for coupling the ocean model to appropriate models of the other components of the climate system (i.e., atmosphere, land surface, and sea ice). Unfortunately, the external coupling interacts with the basic fluid dynamics in complex ways, which precludes the introduction of simple measures of discretization error such as the energy balances discussed in the previous subsections. However, we may still perform multi-resolution analyses in which the same case is integrated using different grids with differing resolutions.

As a take-off point for this test, we cite the previous numerical analyses of Semtner and Chervin [45,46], who performed eddy-resolving simulations of the ocean circulation with Cartesian grids having $\frac{1}{2}^{\circ}$ horizontal

resolution. We used the same 20 vertical levels as employed in these previous studies, which resolved the near-surface region with 25 m grid spacing and gradually coarsened the resolution to 400 m in the deepest part of the ocean, truncating at 5200 m depth. Also, as in Semtner and Chervin [45,46], we began with the ocean at rest, and then relaxed the initially trivial temperature and salinity distributions towards the annually averaged climatology while using the corresponding wind stress data as a surface boundary condition. However, these authors adjusted the time-scale of the dynamics in an artificial, depth-dependent manner in order to accelerate the spin-up, and also performed a succession of other initialization steps that included several modifications of

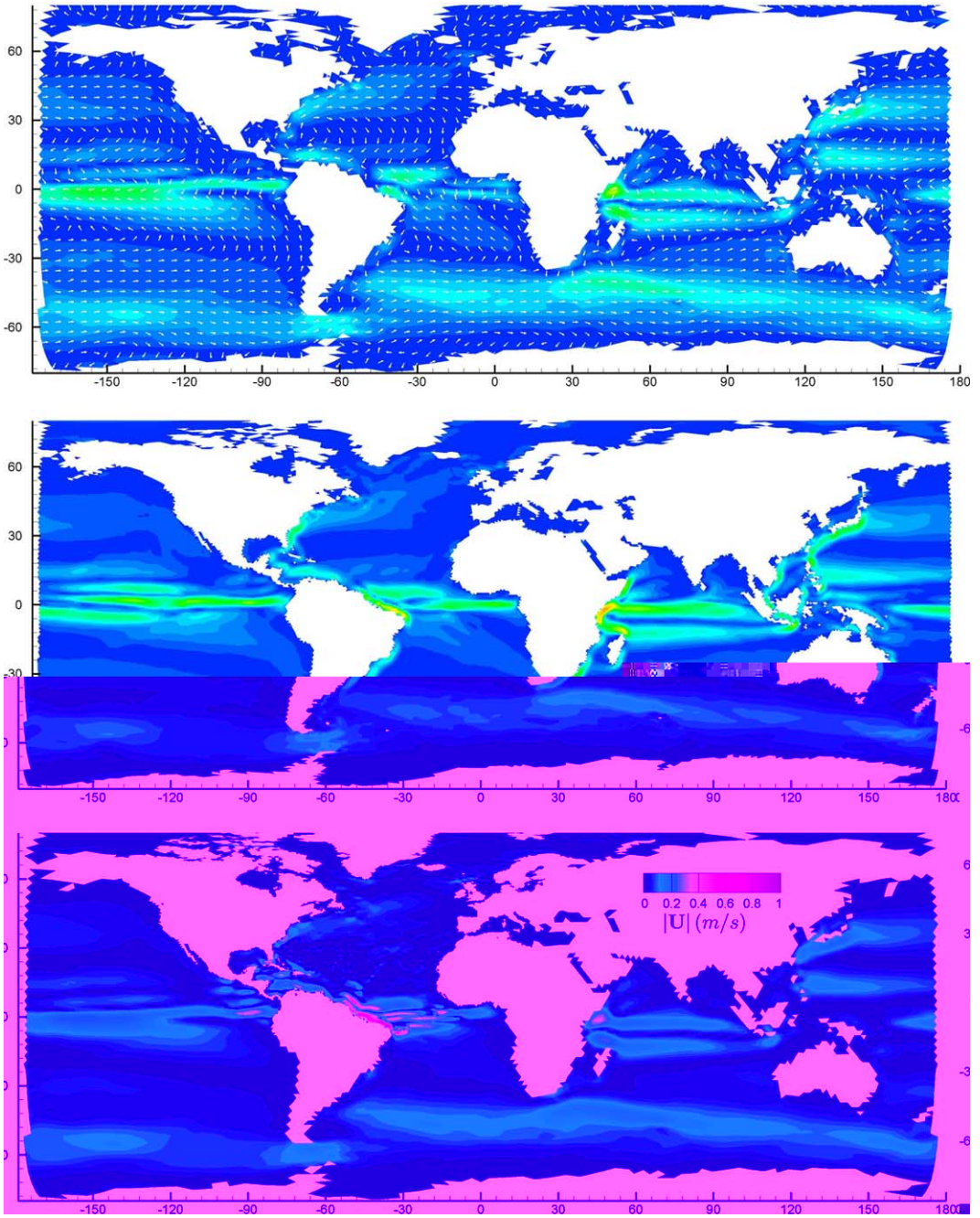

Fig. 10. Velocity vector magnitudes at Z-level $m = 2$ and time $t = 5$ years from three equivalent climatologically forced ocean simulations with different meshes. The top frame also shows the direction of the velocity vector interpolated onto a uniform $5° \times 5°$ grid.

the relaxation scheme and a switch between ∇^2 and ∇^4 dissipation. Their objective was to bring their simulations into a state from which eddies could be marginally resolved at realistic scales in the ocean circulation. In the test for which results are to be provided herein we will not attempt to resolve the mesoscale eddies, but simply to capture the spin-up of the large-scale ocean circulation under a representative relaxation scheme. We therefore invoke no special approximations while relaxing temperature and salinity continuously to their climatological distributions at a time-scale of 1 month at the ocean surface and 1 year in the interior.

In the present test, the heat and salt equations are nonlinearly coupled to the momentum dynamics using the full UNESCO equation of state for seawater (see Gill [47], Appendix III). Because T and S are being directly relaxed to a given climatology on a relatively short time scale, it is not particularly informative to examine them in detail. The same is not true, however, of the velocity field, which equilibrates with the simulation conditions in a non-trivial way over a number of years. In Fig. 10, we show contour plots of the velocity vector magnitude (interpolated to the nodes of the triangular mesh) at Z-level $m = 2$ after 5 years of integration for three cases with different grid structures and resolutions. The plots are in cylindrical projection, and the topmost case also illustrates the velocity directions interpolated onto a uniform $5^\circ \times 5^\circ$ latitude-longitude grid. The results in the top frame are from a case using a uniform grid with about 2° *equatorial* resolution (the triangle edges near the poles are actually the same size as at the equator, but appear distorted because of the convergence of meridians). In the middle frame, the resolution is uniformly doubled to about 1° equatorial equivalent, while in the bottom frame the resolution around the Atlantic basin region is locally quadrupled from the 2° grid to about $\frac{1}{2}^\circ$ equatorial equivalent. All of the velocity fields consistently exhibit the essential circulation pattern of the world ocean, as can be seen in comparison with, for example, Semtner and Chervin [46]. Intense equatorial jets and western boundary currents occur at the correct locations in all of the ocean basins.

Comparing the detailed features of the three cases of Fig. 10, we see the expected result that regions with increased resolution exhibit finer structure in the oceanic jets, along with a corresponding intensification of western boundary currents. At equatorial equivalent $\frac{1}{2}^\circ$ resolution, the most intense boundary currents are on the order of 1 m/s, which is physically appropriate. Typical oceanic gyre currents, whose amplitude is consistently resolved in all the simulations, are on the order of a few centimeters per second. Except around the Atlantic basin, the results in the top and bottom frames are essentially identical, which is to be expected since the resolution of the two simulations is identical over most of the ocean domain. Overall, the results are consistent and as expected. Moreover, these 5 model year simulations show no signs of numerical instability, and further test calculations have been continued for significantly longer periods without problems.

4. Conclusions

The set objective has been achieved: we described a general unstructured grid numerical methodology for hydrostatic dynamics on the sphere, and demonstrated its desirable numerical properties for a number of realistic and artificial simulations with realistic global ocean basin geometry. The methodology has been described and tested with a view to applications in global ocean modeling, and the advantages that it offers are particularly useful in this context. However, the techniques themselves are sufficiently generic to make them relevant also to coastal ocean modeling, atmospheric modeling, and other geophysical applications. Indeed, the present work essentially lays out the basic common elements for a larger unstructured grid climate system model, the development of which is a longer term objective.

With regards to the performance of the new numerical methodology, it has been shown that simulations with fine resolution can be carried out over useful intervals of simulation time. Various aspects of our discretization can incur performance costs, which must be balanced against the benefits, such as the capability to selectively resolve limited regions and the favorable conservation properties. These costs can, however, be systematically controlled in line with the requirements of a particular analysis. We showed how the degree of energy conservation is controlled by the tolerance in the iteration procedure. Another point to consider is that, because of the way in which memory is organized in high-performance vector processors, an unstructured grid model that uniformly resolves the entire sphere will have an inherent performance handicap in comparison with an equivalent Cartesian gridded model at the same resolution. However, this cost also can be circumvented if an application does not require the versatility of a full unstructured grid, for our techniques apply just as well to spherical triangular grids that are describable by simpler ‘‘block structured’’ memory

layouts. An icosahedral grid that has gone through *l uniform* quadtree refinements can, for example, be laid out as $10\ 2^l \times 2^l$ logical square grids, with connectivity information having to be maintained only at the boundaries between these structured blocks (e.g., Stuhne and Peltier [26]). Within each block, there would be no need for indirectly addressed vector operations, which carry a performance penalty. Finally, some of the novel aspects of our space-time discretization might even be adapted to existing curvilinear Cartesian grids, with the aim of improving conservation properties.

Given the large number of dependencies upon specialized areas of research, it would be impossible at the outset to develop and present a complete model that would be competitive in every way with state-of-the-art existing models. The key novelties at the present stage of the work are in the spherical hydrostatic unstructured grid techniques – specifically, in the application of robust, stable, energy-conserving time-stepping schemes on layered spherical triangular tessellations. The advantages and present limitations of these numerical methods have been analyzed in the context of a prototype model whose various components can be improved with the assimilation of advances in specialized areas. We have mentioned already the desirability of developing mesh generation techniques that optimize accuracy while better representing coastlines, as well as the availability of alternative mixing and eddy parameterization schemes for unresolved dynamics. Another area for possible future research relates to the linear inversion scheme for advancing model time, which could potentially be accelerated with better preconditioning schemes for the GMRES solver, or with the use of a multigrid version of this algorithm. In relation to the model physics, the discretization can be extended to non-hydrostatic Boussinesq and anelastic dynamics. This would open the door to a range of more exotic applications, such as simulations of astrophysical processes and of convection in the Earth's mantle.

Our highest priority for future research is to incorporate elements that are required for the most demanding oceanic applications. One clear requirement is the incorporation of a dynamic free surface as an alternative to the rigid-lid approximation. In and of itself, this would be relatively straightforward and would carry very little additional computational expense in our model, as we already employ implicit time-stepping (which is more-or-less required in practice because of the very high phase speed of the gravity wave mode associated with the oscillation of the free surface). However, in order to fully exploit the geometric versatility offered by unstructured grid methods, a better approach would at the same time combine the discretization of the spherical shell with a transformation of the radial coordinate (e.g., Wedi and Smolarkiewicz [48]). In tandem with the above-discussed optimization of the horizontal meshing scheme, this would provide, overall, for a superior representation of the ocean domain geometry. When such a capability is in place, it will be possible to achieve new insights into the dynamics of small-scale and geometry-dependent hydrodynamic phenomena in the context of the global ocean circulation – for instance, in order to investigate tidal dynamics and the detailed role of eddies in coastal boundary currents.

Acknowledgements

The work reported in this paper has been supported by the Polar Climate Stability network which is financed by the Canadian Foundation for Climate and Atmospheric Sciences together with a consortium of Canadian universities.

References

[1] K. Bryan, A numerical model for the study of the world ocean, J. Comput. Phys. 4 (1969) 347–376.
[2] K. Bryan, M.D. Cox, The circulation of the world ocean: a numerical study. Part I, a homogeneous model, J. Phys. Oceanogr. 2 (1972) 319–335.
[3] A.J. Semtner, History and methodology of modeling the world ocean, in: J.J. O'Brien (Ed.), Advanced Physical Oceanographic Numerical Modeling, D. Reidel, Norwell, Mass, 1986, pp. 23–32.
[4] S.M. Griffies, Fundamentals of Ocean Climate Models, Princeton University Press, Princeton, NJ, 2004.
[5] R.J. Murray, Explicit generation of orthogonal grids for ocean models, J. Comput. Phys. 126 (1996) 251–273.
[6] P.G. Myers, A.J. Weaver, A diagnostic barotropic finite-element ocean circulation model, J. Atmos. Oceanic Technol. 12 (1995) 511–526.
[7] D.R. Lynch, J.T.C. Ip, C.E. Naimie, F.E. Werner, Comprehensive coastal circulation model with application to the Gulf of Maine, Continent. Shelf Res. 16 (1996) 875–906.
[8] V. Casulli, R.A. Walters, An unstructured grid, three-dimensional model based on the shallow water equations, Int. J. Numer. Meth. Eng. 32 (2000) 331–348.

[9] C. Chen, H. Liu, R.C. Beardsley, An unstructured grid, finite-volume, three-dimensional, primitive equations ocean model: application to coastal ocean and estuaries, J. Atm. Oceanic Technol. 20 (2003) 159–186.
[10] D. Nechaev, J. Schröter, M. Yaremchuk, A diagnostic stabilized finite-element ocean circulation model, Oceanic Model. 5 (2003) 37–63.
[11] Y. Zhang, E.P.I. Baptista, António M. Myers, A cross-scale model for 3D baroclinic circulation in estuary-plume-shelf systems: I. Formulation and skill assessment, Continent. Shelf Res. 24 (2004) 2187–2214.
[12] National Geophysical Data Center (NGDC), 2-Minute Gridded Global Relief Data (ETOPO2). Available from: URL: <www.ngdc.noaa.gov/mgg/global/relief/ETOPO2>.
[13] W.R. Peltier, L.P. Solheim, The climate of the earth at last glacial maximum: statistical equilibrium state and a mode of internal variability, Quatern. Sci. Rev. 23 (2004) 335–357.
[14] F.H. Harlow, J.E. Welch, Numerical calculations of time dependent viscous incompressible flow of fluid with a free surface, Phys. Fluids 8 (1965) 2182–2188.
[15] D.K. Lilly, On the computational stability of numerical solutions of time-dependent non-linear geophysical fluid dynamics problems, Mon. Weather Rev. 93 (1965) 11.
[16] B. Perot, Conservation properties of unstructured staggered mesh schemes, J. Comput. Phys. 159 (2000) 58–89.
[17] X. Zhang, D. Schmidt, B. Perot, Accuracy and conservation properties of a three-dimensional unstructured staggered mesh scheme for fluid dynamics, J. Comput. Phys. 175 (2002) 764–791.
[18] R.A. Nicolaides, The covolume approach to computing incompressible flow, in: M.D. Gunzburger, R.A. Nicolaides (Eds.), Incompressible Computational Fluid Dynamics, Cambridge University Press, Cambridge, UK, 1993, p. 295.
[19] K. Bryan, M.D. Cox, A nonlinear model of an ocean driven by wind and differential heating: part I. Description of the three-dimensional velocity and density fields, J. Atmos. Sci. 25 (1968) 945–967.
[20] V. Frayss, L. Giraud, S. Gratton, J. Langou, A Set of GMRES Routines for Real and Complex Arithmetics, Tech. Rep. TR/PA/03/3, CERFACS, public domain software Available on: <www.cerfacs.fr/algor/Softs> (2003).
[21] D.L. Williamson, J.B. Drake, J.J. Hack, R. Jakob, P.N. Swarztrauber, A standard test set for numerical approximations to the shallow water equations in spherical geometry, J. Comput. Phys. 102 (1992) 211–224.
[22] J. Côté, A Lagrange multiplier approach for the metric terms of semi-Lagrangian models on the sphere, Quart. J.R. Met. Soc. 114 (1988) 1347.
[23] T.S. Lau, S.H. Lo, Finite element mesh generation over analytical curved surfaces, Comp. Struct. 59 (1996) 301–309.
[24] D.M. Greaves, A.G.L. Borthwick, Hierarchical tree-based finite element mesh generation, Int. J. Numer. Meth. Eng. 45 (1999) 447–471.
[25] J.R. Baumgardner, P.O. Frederickson, Icosahedral discretization of the two-sphere, Siam J. Numer. Anal. 22 (1985) 1107.
[26] G.R. Stuhne, W.R. Peltier, Vortex erosion and amalgamation in a new model of large scale flow on the sphere, J. Comput. Phys. 128 (1996) 58–81.
[27] G.R. Stuhne, W.R. Peltier, New icosahedral grid-point discretizations of the shallow water equations on the sphere, J. Comput. Phys. 148 (1999) 23–58.
[28] A. Arakawa, Computational design for long-term numerical integration of the equations of fluid motion: Two-dimensional incomressible flow. Part I, J. Comput. Phys. 1 (1966) 119–143.
[29] J.K. Dukowicz, R.D. Smith, Implicit free-surface method for the Bryan–Cox–Semtner ocean model, J. Geophys. Res. 99C (1994) 7991–8014.
[30] R. Löhner, C. Yang, E. Oñate, S. Idelssohn, An unstructured grid-based, parallel free surface solver, Appl. Num. Meth. 31 (1999) 271–293.
[31] K. Mahesh, G. Constantinescu, P. Moin, A numerical method for large-eddy simulation in complex geometries, J. Comput. Phys. 197 (2004) 215–240.
[32] V. Casulli, R.T. Cheng, A semi-implicit finite difference model for three-dimensional tidal circulation, in: M.L. Spaulding (Ed.), Estuarine and Coastal Modeling: Proceedings of the 2nd International Conference, Americal Society of Civil Engineers, 1992, pp. 620–631.
[33] K. Bryan, S. Manabe, R.C. Pacanowski, A global ocean–atmosphere climate model. Part II. The oceanic circulation, J. Phys. Oceanogr. 5 (1975) 30–46.
[34] R.J. Murray, C.J.C. Reason, A curvilinear ocean model using a grid regionally compressed in the South India ocean, J. Phys. Oceanogr. 31 (2001) 2809–2823.
[35] R.M. Clancy, A note on finite differencing of the advection-diffusion equation, Mon. Weather Rev. (1981) 1807–1809.
[36] R.C. Pacanowsky, S.G.H. Philander, Parameterization of vertical mixing in numerical models of tropical oceans, J. Phys. Oceanogr. 11 (1981) 1443–1451.
[37] M.A. Hallworth, H.E. Huppert, M. Ungarish, Axisymmetric gravity currents in a rotating system: experimental and numerical investigations, J. Fluid Mech. 447 (2001) 1–29.
[38] A. Stegner, P. Bouruet-Aubertot, T. Pichon, Nonlinear adjustment of density fronts. Part 1. The Rossby scenario and the experimental reality, J. Fluid Mech. 502 (2004) 335–360.
[39] S.M. Polavarapu, W.R. Peltier, The structure and nonlinear evolution of synoptic scale cyclones: life cycle simulations with a cloud-scale model, J. Atmos. Sci. 47 (1990) 2645–2672.
[40] Y.H. Yamazaki, W.R. Peltier, The existence of subsynoptic-scale baroclinic instability and the nonlinear evolution of shallow disturbances, J. Atmos. Sci. 58 (2001) 657–683.

[41] A.B.G. Bush, J.C. McWilliams, W.R. Peltier, The formation of oceanic eddies in symmetric and asymmetric jets. Part I: Early time evolution and bulk eddy transports, J. Phys. Oceanogr. 25 (1995) 1959–1979.
[42] A.B.G. Bush, J.C. McWilliams, W.R. Peltier, The formation of oceanic eddies in symmetric and asymmetric jets. Part II: late time evolution and coherent vortex formation, J. Phys. Oceanogr. 26 (1996) 1825–1848.
[43] S. Levitus, World Ocean Atlas, Tech. Rep. 13, National Oceanographic Data Center, CD-ROM data set (1994).
[44] S. Hellerman, M. Rosenstein, Normal monthly wind stress over the world ocean with error estimates, J. Phys. Oceanogr. 13 (1983) 1093–1104.
[45] A.J. Semtner, R.M. Chervin, A simulation of the global ocean circulation with resolved eddies, J. Geophys. Res. 93C (1988) 15502–15522.
[46] A.J. Semtner, R.M. Chervin, Ocean general circulation from a global eddy-resolving model, J. Geophys. Res. C 97 (1992) 5493–5550.
[47] A.E. Gill, Atmosphere–Ocean DynamicsInternational Geophysics Series, vol. 30, Academic Press, San Diego, 1982.
[48] N.P. Wedi, P.K. Smolarkiewicz, Extending Gal-Chen and Somerville terrain-following coordinate transformation on time-dependent curvilinear boundaries, J. Comput. Phys. 193 (2003) 1–20.